A systematic analysis of the broad iron Kα line in neutron-star LMXBs with *XMM-Newton*⋆

C. Ng[1], M. Díaz Trigo[2], M. Cadolle Bel[3], and S. Migliari[1]

[1] ESAC, PO Box 78, 28691 Villanueva de la Cañada, Madrid, Spain
[2] *XMM-Newton* Science Operations Centre, Science Operations Department, ESAC, PO Box 78, 28691 Villanueva de la Cañada, Madrid, Spain
e-mail: mdiaz@sciops.esa.int
[3] Integral Science Operations Centre, Science Operations Department, ESAC, PO Box 78, 28691 Villanueva de la Cañada, Madrid, Spain

ABSTRACT

We analysed the *XMM-Newton* archival observations of 16 neutron star (NS), low-mass X-ray binaries (LMXBs) to study the Fe K emission in these objects. The sample includes all the observations of NS LMXBs performed in EPIC pn timing mode with *XMM-Newton* publicly available until September 30, 2009. We performed a detailed data analysis considering pile-up and background effects. The properties of the Fe lines differed from previous published analyses because of either incorrect pile-up corrections or different continuum parameterisation. Eighty percent of the observations for which a spectrum can be extracted showed significant Fe line emission. We found an average line centroid of 6.67 ± 0.02 keV and a finite width, σ, of 0.33 ± 0.02 keV. The equivalent width of the lines varied between 17 and 189 eV, with an average weighted value of 42 ± 3 eV. For sources where several observations were available, the Fe line parameters changed between observations whenever the continuum changed significantly. The line parameters did not show any correlation with luminosity. Most important, we could fit the Fe line with a simple Gaussian component for all the sources. The lines did not show the asymmetric profiles that were interpreted as indicating relativistic effects in previous analyses of these LMXBs.

Key words. accretion, accretion disks – X-rays: binaries – X-rays: general

1. Introduction

Accreting binaries often show Fe line emission in their X-ray spectra. The ability of *Chandra*, *XMM-Newton*, *Suzaku* and *Swift* to obtain medium- to high-resolution spectra covering the Fe K energy band has opened a new era in the observations of stellar-mass black holes (BHs) and NS binaries. The large effective area of these observatories is crucial for detecting Fe line emission, while the high resolution enables us to distinguish between narrow and intrinsically broad features. Broad Fe lines are also present in active galactic nuclei (Tanaka et al. 1995; Nandra et al. 1997), though studies of large samples of sources show that the average fraction of broad Fe lines is never higher than 40% (Guainazzi et al. 2006; Nandra et al. 2007).

The origin of broad Fe lines has been extensively discussed (e.g. Sunyaev & Titarchuk 1980; Fabian et al. 1989; Done et al. 2007; Ross & Fabian 2007; Titarchuk et al. 2009). However, even after the advent of the current powerful X-ray observatories, the exact determination of the line width and the mechanisms responsible for it are still controversial. Undoubtedly, the most exciting possibility is that such lines originate in the disc close to the BH event horizon or to the NS by fluorescent emission following illumination (and photoinisation) of the accretion disc by an external source of X-rays (Reynolds & Nowak 2003; Fabian & Miniutti 2005; Matt 2006). In this model, the combination of relativistic Doppler effects arising from the high orbital

velocities and gravitational effects of the strong gravitational field in the vicinity of the compact object smear the reflected features. In this case, detailed X-ray spectroscopy of Fe line features can be used to study Doppler and gravitational redshifts, thereby providing key information on the location and kinematics of the material in the vicinity of the compact object. Most interesting of all is the potential for establishing BH spin using relativistic Fe Kα lines. The spin value is constrained mainly by the lower boundary of the broad line, which depends on the inner boundary of the disc emission (identified with the marginally stable orbit) where the gravitational redshift is maximal. Therefore, lines that are strongly skewed toward lower energies can indicate black hole spin (Miller et al. 2009; Hiemstra et al. 2009; Reis et al. 2009).

The recent claim of broad skewed Fe lines from NS binaries has opened the exciting possibility of determining an upper limit to the radius of the NS, the most difficult parameter to obtain to constrain the equation of state of NSs (Bhattacharyya & Strohmayer 2007). The advantage of using Fe K emission lines as a probe of the NS radius is that they only require short observations to clearly reveal the relativistic lines, and do not require any knowledge of the distance to the object.

An alternative location for the line-emitting region could be the inner part of the so-called accretion disc corona (ADC), formed by evaporation of the outer layers of the disc illuminated by the emission of the central object (e.g., White & Holt 1982). In the corona, where the gas is highly ionised, the Fe line emission is likely to come from recombination onto hydrogenic

and helium-like Fe. In the region below the transition region, the Fe will be ionised at most a few times and fluorescence will be the dominant process (Kallman & White 1989). In the corona, Compton scattering will broaden and shift the centroid of the line. The line broadening and shift are due to Doppler and/or recoil effects, depending on the temperature of the plasma compared to the energy of the photons (Pozdnyakov et al. 1979; Sunyaev & Titarchuk 1980). The final line width is determined by the simultaneous effects of blending, Compton scattering, and rotation. For a value of $f \sim 0.1$ (f being the fraction of the incident X-ray flux, which is assumed to penetrate the base of the hot medium or corona), Kallman & White (1989) calculated a centroid energy of $6.6-6.7$ keV for the Fe line and a width of ~ 0.6 keV at small radii ($R \lesssim 10^8$ cm). For $f \sim 1$, the width can be as much as ~ 1 keV (*FWHM*). Alternatively, the widths of ~ 1 keV can also be attained via emission from a photoionised gas with large Thomson depth ($\tau \gtrsim 3$). Such large Compton depths could arise if the corona is heated by some mechanism other than X-rays, or if the line of sight of the observer through the corona were very different from that of the compact X-ray source (Kallman & White 1989).

A third scenario for the formation of broad Fe lines in LMXBs could be one where extensive red wings form by recoil of line photons in an optically thick medium expanding, or converging, at relativistic velocities (Titarchuk et al. 2003; Laming & Titarchuk 2004; Laurent & Titarchuk 2007). It is assumed that the wide-open wind is launched at some disc radius where the local radiation force presumably exceeds the local disc gravity. The wind should be illuminated by the emission of X-rays formed in the innermost part of the source. The Kα line is generated in a narrow wind shell, and the line profile is formed in the partly ionised wind when Kα line photons are scattered off the diverging flow (wind) electrons (Titarchuk et al. 2009). The red-skewed part of the spectrum is formed by photons undergoing multiple scatterings, while the primary peak is formed by photons escaping directly to the observer.

The line properties of an ADC are in general expected to be different from those of an accretion disc (Brandt & Matt 1994). In the former case, the equivalent width (*EW*) is nearly independent of inclination except at very high angles (Vrtilek et al. 1993), while the dependence on inclination in the case of an accretion disc is significant (Brandt & Matt 1994). Therefore Fe lines appear to be a powerful tool for distinguishing between an ADC, an accretion disc, or any other origin of the Fe line in LMXBs. Proper modelling of the Fe line is mandatory to determine the unique origin of the line and, in the case of relativistic broadened Fe lines, to derive the spin of the BH or an upper limit to the radius of the NS.

White et al. (1986) performed a systematic analysis of six NS LMXBs with EXOSAT and found line emission in 83% of the objects. The lines were broad with *FWHM* of $0.8-1.3$ keV and had centroid energies of $6.6-6.9$ keV. Furthermore, the line properties did not show any obvious correlation with luminosity. This led White et al. (1986) to conclude that the only plausible broadening mechanism was Comptonisation in a cloud with a Thomson depth of a few and an electron temperature close to 7 keV. Hirano et al. (1987) analysed ten NS LMXBs observed with *Tenma* and found line emission from six of them. The line energy had a weighted average of 6.66 ± 0.05 keV with *EW*s in the range $20-60$ eV. A significant line width of 0.55 keV was only obtained for one source, though a width of ~ 1 keV could not be rejected for the other cases. They attributed the line emission to recombination processes in the accretion-disc corona and explained its width as Compton scattering in the region with

an optical depth of 1 and an average temperature ~ 1 keV. Asai et al. (2000) extended the analysis of the Fe K emission lines to twenty NS LMXBs observed with ASCA. They detected significant Fe lines from about half of the sources. The average properties of the lines were a line centre of 6.56 keV and a finite width of ~ 0.5 keV (*FWHM*) in six of the sources. They also found a large scatter in the *EW* of the detected lines, ranging between 10 and 170 eV. They concluded that the Fe K lines are likely produced through the radiative recombination of photoionised plasma and explained the line width as a combination of line blending, Doppler broadening, and Compton scatterings.

The picture outlined by the analyses based on EXOSAT, *Tenma* and ASCA data changed with recent analyses of observations of NS LMXB observations by *XMM-Newton*, *Chandra* and *Suzaku*. Several skewed Fe lines have been claimed, and their origin attributed to relativistic effects (e.g., Bhattacharyya & Strohmayer 2007; Papitto et al. 2009; Di Salvo et al. 2009; D'Aì et al. 2009) or to Compton scattering in an optically thick medium expanding, or converging, at relativistic velocities (e.g., Laurent & Titarchuk 2007; Titarchuk et al. 2009). However, only some of the NS LMXBs have shown such asymmetric lines, while others show symmetric lines (e.g., Cackett et al. 2008). A systematic analysis of the Fe K lines is at this stage fundamental for establishing why some sources exhibit skewed lines while others show symmetric lines or why lines are only present in some of the sources. Having an answer to these questions would help clarify the currently controversial origin of the lines.

With this aim we performed a systematic analysis of all the NS LMXBs observed by *XMM-Newton* since the beginning of the mission and publicly available up to September 30, 2009. We excluded from this sample observations of dipping or ADC sources, i.e. with known inclinations above $70°$, since their analyses at the Fe band are complicated by strong absorption in the line of sight. We chose *XMM-Newton* to perform this study for the following reasons. Firstly, its high effective area both below and above the Fe K band allows a good determination of the shape and width of the Fe line as well as the continuum. Secondly, *XMM-Newton* has provided most of the detections and well-determined profiles of broad Fe lines. Finally, after 10 years of operation, *XMM-Newton* has an ample archive of public data which can be used to determine class properties in the least biased way.

In total we analysed 26 observations of 16 sources from the *XMM-Newton* archive. We restricted our analysis to sources observed in the EPIC pn timing mode. This mode is specially suited to observation of bright sources. Therefore, by selecting all the observations performed in this mode we obtained a sample of spectra with the best possible statistics.

In what follows we first present the properties of the selected sample and our analysis method. Special attention has been paid to eliminate pile-up effects and to the treatment of background. Then, we performed spectral fitting accounting for the excess emission at the Fe K energy band. We finally discuss the implications of our analysis regarding the characteristics of the lines and their possible origin. In an appendix we compare the characteristics of the lines in this work with previous analyses of the same observations and discuss the reason for any discrepancies that were found.

2. Observations and data reduction

The *XMM-Newton* Observatory (Jansen et al. 2001) includes three 1500 cm^2 X-ray telescopes, each with an EPIC ($0.1-15$ keV) at the focus. Two of the EPIC imaging

spectrometers use MOS CCDs (Turner et al. 2001), and one uses pn CCDs (Strüder et al. 2001). The RGSs (0.35−2.5 keV, Den Herder et al. 2001) are located behind two of the telescopes. In addition, there is a co-aligned 30 cm diameter Optical/UV Monitor telescope (OM, Mason et al. 2001) that provides simultaneously coverage with the X-ray instruments. Data products were reduced using the Science Analysis Software (SAS) version 9.0. The EPIC MOS cameras were not used in most of the observations analysed in this paper because their telemetry was allocated to the EPIC pn camera to avoid Full Scientific Buffer in the latter. Since the pn has an effective area ∼5 times higher at 7 keV than the MOS CCDs and the latter were not available for most of the observations, we present only the analysis of the EPIC pn data here. We did not analyse the RGS data since they do not cover the Fe K energy band in which we are interested.

Table 1 is a summary of the *XMM-Newton* observations. The EPIC pn was used in timing mode for all the observations. In this mode only one CCD chip is operated, and the data are collapsed into a one-dimensional row (4′.4) and read out at high speed, with the second dimension replaced by timing information. This allows a time resolution of 30 μs. We used the SAS task epfast on the event files to correct for a charge transfer inefficiency (CTI) effect seen in the EPIC pn timing mode when high count rates are present[1]. Ancillary response files were generated using the SAS task arfgen following the recommendations of the *XMM-Newton SAS User Guide*[2] for piled-up observations in timing mode whenever applicable. Response matrices were generated using the SAS task rmfgen. We extracted one EPIC pn spectrum per observation, not taking any intra-observational variability into account (see Sect. 3.1). Bursts were excluded for the calculation of the total energy spectra whenever present.

Light curves were generated with the SAS task epiclccorr, which accounts for time-dependent corrections within a exposure, such as dead time and GTIs.

2.1. Pile-up treatment

Since the average count rate in the EPIC pn was close to, or above, the 800 counts s^{-1} level at which pile-up effects may become significant for at least eight observations in the sample, we investigated the presence of pile-up in detail before extracting the spectra. We used the SAS task epatplot, which utilises the relative ratios of single- and double-pixel events deviating from the standard values as a diagnostic tool in case of significant pile-up in the pn camera timing mode. We found that the spectra of twelve observations from eight sources were affected by pile-up (see Table 1).

Then, we extracted several spectra selecting single and double timing mode events (patterns 0 to 4) and different spatial regions for each of the piled-up observations. For 4U 1705−44 (Obs 0551270201), 4U 1636−536, 4U 1735−44, and GX 9+9 (Obs 0090340601), the source coordinates fell into the centre of the central column of the CCD. Therefore, source events were first extracted from a 64″ (15 columns) wide box centred on the source position (Region 1). Then, we excluded the neighbouring 1, 3, 5, and 7 columns from the centre of Region 1 (Regions 2−5, respectively) and extracted one spectrum for each

of the defined regions. For GX 340+0, GX 349+2, Ser X−1, and GX 9+9 (Obs 0090340101) the source fell between two columns in the CCD. Therefore, source events were first extracted from a 68″ (16 columns) wide box centred on the source position (Region 1), and Regions 2−5 were defined by excluding 2, 4, 6, and 8 columns respectively from the centre of Region 1. This was done to preserve the best symmetry when excluding piled-up events. Table 1 lists the number of columns that had to be extracted from each source, in order to obtain spectra free of pile-up. It is evident that pile-up already starts to be important at a count rate of ≳450 s^{-1}. Pile-up depends on the spectral shape and the time variation of the source in a complex way. Therefore, although the average count rate of an observation generally indicates whether the effects of pile-up are important, it is also of *utmost* importance to carefully inspect the epatplot to evaluate the PSF radius at which the relative ratios of single- and double-pixel events do not deviate from the standard values in the full energy band.

As an example of the use of epatplot to determine the amount of pile-up, we show the epatplots in a highly piled-up source, GX 349+2, and in a dim source free of pile-up, 4U 1728−34, in Appendix A.

2.2. Background treatment

In the EPIC pn timing mode, there is no source-free background region, since the PSF of the telescope extends further than the central CCD boundaries. The central CCD has a field of view of 13′.6 × 4′.4 in the pn. In timing mode, the largest column is the one in which the data are collapsed into one-dimensional row. Therefore, the maximum angle for background extraction is 2′, compared to 5′ for imaging modes. In our sample, sixteen out of the nineteen observations (for which source emission is detected) are very bright, with total count rates ≳200 s^{-1} (see Table 1). Therefore, the spectra from these sources will not be significantly modified by the "real" background, which contributes less than 1% to the total count rate in most of the bandwidth. Conversely, subtracting the background extracted from the outer columns of the central CCD will modify the source spectrum, since the PSF is energy dependent and the source photons scattered to the outer columns do not show the same energy dependence as the photons focused on the inner columns.

For the reasons mentioned above, in this work we chose not to subtract the "background" extracted from the outer regions of the central CCD. This is an appropriate method for all the sources where the "real" background is negligible compared to the source count rate at all energies. In contrast, for sources with $N_\mathrm{H} \gtrsim 1 \times 10^{22}$ atom cm^{-2}, the background is expected to contribute significantly at energies ≲1 keV, where most of the source photons are absorbed in the interstellar medium. Therefore for these sources, it is mandatory to remove the bins where the background is significant before spectral analysis.

With this aim, we extracted the background from the outer regions of the central CCD of "blank fields", where we took as examples of "blank fields" the observations of Aql X−1 and 4U 1608−52 listed in Table 1 for which the source was not significantly detected. Then, we inspected the spectra of sources with $N_\mathrm{H} \gtrsim 0.5 \times 10^{22}$ atom cm^{-2}, and compared the "blank field" background with the background extracted from the observation for which the source was being analysed. We scaled the former so that it was comparable to the latter at energies where we did not expect a significant flux from the source. We estimated such energy as the one at which simulated spectra with different values of N_H started to flatten as a consequence of being

---

[1] More information about the CTI correction can be found in the *EPIC status of calibration and data analysis* and in the current calibration file (CCF) release note *Rate-dependent CTI correction for EPIC-pn timing modes*, by Guainazzi et al. (2008), at http://xmm.esac.esa.int/external/xmm_calibration

[2] http://xmm.esac.esa.int

Table 1. *XMM-Newton* archival observations of NS LMXBs performed in EPIC pn timing mode ordered by right ascension.

Source	Class	Observation ID	Observation times (UTC) Start (year mon day)	(hr:mn)	End (hr:mn)	T (ks)	C [σ] (s^{-1})	Pile-up	Columns removed
4U 0614+09	A,UCXB	0111040101	2001 Mar. 13	12:27	17:11	10	240 [8]	N	0
Cen X−4	T	0144900101	2003 Mar. 01	15:11	14:48	–	–	–	–
4U 1543−62	UCXB	0061140201	2001 Feb. 04	13:16	03:13	46	203 [5]	N	0
4U 1608−52	A, T	0074140101	2002 Feb. 13	16:04	20:57	–	–	–	–
		0074140201	2002 Feb. 15	01:34	06:22	–	–	–	–
4U 1636−536	A	0303250201	2005 Aug. 29	17:47	02:47	29	243 [15]	N	0
		0500350301	2007 Sep. 28	15:07	00:17	19	507 [11]	Y	1
		0500350401	2008 Feb. 27	03:38	15:01	37	652 [24]	Y	3
GX 340+0	Z	0505950101	2007 Sep. 02	12:40	02:34	40	801 [50]	Y	8
GX 349+2	Z	0506110101	2008 Mar. 19	15:07	23:00	7	2043 [69]	Y	8
4U 1705−44	A	0402300201	2006 Aug. 26	04:27	14:57	35	30 [1]	N	0
		0551270201	2008 Aug. 24	01:41	17:15	45	742 [31]	Y	7
GX 9+9	A	0090340101	2001 Sep. 04	09:37	15:17	1	1380 [11]	Y	4
		0090340601	2002 Sep. 25	09:15	16:10	5	1458 [25]	Y	5
4U 1728−34	A	0149810101	2002 Oct. 03	21:48	05:55	26	88 [1]	N	0
4U 1735−44	A	0090340201	2001 Sep. 03	02:57	09:06	5	1198 [23]	Y	3
Ser X−1	A	0084020401	2004 Mar. 22	14:58	21:18	6	1074 [23]	Y	4
		0084020501	2004 Mar. 24	14:47	21:10	7	925 [14]	Y	4
		0084020601	2004 Mar. 26	14:18	20:41	5	1014 [32]	Y	4
Aql X−1	A, T	0112440101	2002 Oct. 27	01:03	03:30	–	–	–	–
		0112440301	2002 Oct. 15	01:55	04:17	–	–	–	–
		0112440401	2002 Oct. 17	01:42	05:52	–	–	–	–
		0303220201	2005 Apr. 07	14:30	18:58	3	228 [6]	N	0
IGR J00291+5934	AMXP, T	0560180201	2008 Aug. 25	04:45	14:25	–	–	–	–
XTE J1807−294	AMXP, T	0157960101	2003 Mar. 22	13:40	18:40	9	41 [1]	N	0
SAX J1808.4−3658	AMXP, T	0560180601	2008 Sep. 30	23:15	17:19	43	550 [10]	Y^a	2

Notes. T is the total effective EPIC pn exposure time. C is the pn 0.7–10 keV persistent emission count rate after dead time correction, calculated as the mean of the Gaussian function used to fit the count rate distribution (σ represents the standard deviation of the distribution). The source class is A (atoll), Z (Z source), UCXB (ultra-compact X-ray binary), or AMXP (accreting millisecond X-ray pulsar). T means transient system. The last column shows the number of columns excised from the centre of the PSF to remove the pile-up effects in spectral analysis. $^{(a)}$ For SAX J1808.4−3658, we found indications of very small pile-up in the two central columns. Therefore we present the analysis with both the full PSF and after removal of the 2 central columns in the following sections.

dominated by background events. Then we removed energy bins where we expect a contribution from the background to the total count rate of more than 1%. For 4U 1705−44, 4U 1728−34, and GX 340+0, we removed bins below 1.5, 1.8, and 2.2 keV, respectively. We used all the other spectra from 0.7 keV up to 10 keV.

To illustrate the effects of background subtraction in the spectral fitting and to evaluate the validity of our method, we chose the weakest and brightest sources of our sample, 4U 1705−44 (Obs 0402300201) and GX 349+2. We examined the differences in the spectra after (1) not subtracting any background from the source spectrum (Spec 1); (2) subtracting the background extracted from a blank field (Spec 2); and (3) subtracting the background extracted from the outer columns of the central CCD during the observation (Spec 3). Figure 1 (left panels) shows the ratio of Spec 1 to its best-fit continuum model (black) and the difference from Specs 2 and 3 with respect to the same model. The red and black residuals are consistent within the errors at all energies for GX 349+2 (lower panels) and above ∼1 keV for 4U 1705−44 (upper panels). The deviation below ∼1 keV for 4U 1705−44 is expected, since at such energies the background photons make a significant contribution to the total spectrum. In contrast, we observe an energy-dependent discrepancy of Spec 3 with respect to Specs 1 and 2, as expected from the energy dependence of the PSF. These results are consistent with the shape of the background shown in Fig. 1 (right panels).

The "background" extracted from the outer columns of the CCD is clearly contaminated by the source at all energies (compared to the source spectrum), while the "background" extracted from a blank field shows the shape expected when compared to Fig. 35 of the *XMM-Newton Users Handbook*.

3. Light curves and spectral fitting

3.1. Light curves

Figure 2 shows EPIC pn light curves and hardness ratios of all the *XMM-Newton* observations analysed in this paper with a binning of 64 s. The hardness ratio is obtained by dividing the number of counts in the 3−10 keV energy range by those in the 0.7−3 keV energy range, except for 4U 1705−44, 4U 1728−34 and GX 340+0, for which the soft band is 1.5−3 keV, 1.8−3 keV and 2.2−3 keV, respectively. The light curves of observations with count rates ≳200 counts s^{-1} suffer from regular telemetry drops that are seen when the light curves are plotted with a high time resolution, e.g. 1 s. The SAS task `epiclccorr` accounts for such gaps, as well as for dead time with a different origin, by taking the count rate in adjacent frames into account (see Sect. 2).

The average count rate changed by more than 2 orders of magnitude among the studied sources. Observations of the same source taken within months showed strong variability in some
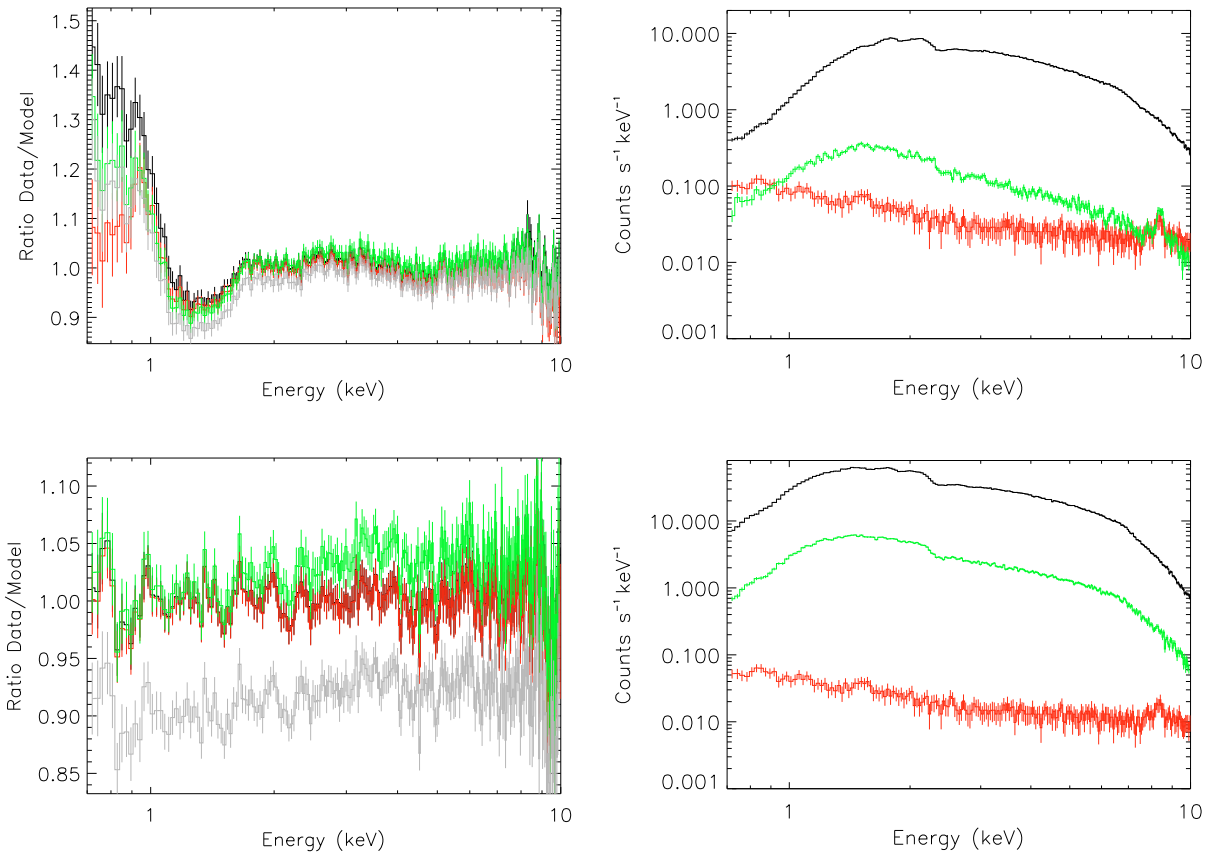
Fig. 1. *Left*: ratio of Spec 1 (see Sect. 2.2) to its best-fit continuum model (black) and the difference from Spec 2 (red) and Spec 3 (green) with respect to the same model. Spec 3 has been scaled so that the energy bin at 10 keV coincides with Spec 1. The original Spec 3 is shown in grey. *Right:* Source spectrum (black), background from a blank field (red), and background extracted from the outer columns of the central CCD (green). The upper and lower panels show the results for 4U 1705−44 and GX 349+2, respectively.

cases (e.g. 4U 1636−536) and a steady level in others (e.g. Ser X−1).

Strong variability of ≳30% within one observation is only present in the light curves of GX 340+0 and GX 349+2. The variabilities within such observations were studied by D'Aì et al. (2009) and Iaria et al. (2009), who find that the spectral fits to different intervals within the observations gave consistent results for the parameters of the Fe line.

3.2. X-ray spectra

We rebinned the EPIC pn spectra to over-sample the *FWHM* of the energy resolution by a factor of 3 and to have a minimum of 25 counts per bin, to allow the use of the χ^2 statistic. To account for systematic effects in the EPIC pn timing mode, we added a 2% uncertainty quadratically to each pn spectral bin. We performed spectral analysis using XSPEC (Arnaud 1996) version 12.3.1. We used the photo-electric cross-sections of Wilms et al. (2000) to account for absorption by neutral gas with solar abundances (the so-called `tbabs` XSPEC model). Spectral uncertainties are given at 90% confidence ($\Delta\chi^2 = 2.71$), and upper limits at 95% confidence.

We first fitted the EPIC pn spectra with a model consisting of a blackbody and a disc blackbody, both modified by photo-electric absorption from neutral material (model `tbabs*(bbodyrad+diskbb)` in XSPEC). The fits were unacceptable in most of the cases, mainly owing to the broad

emission feature at ∼6−7 keV and a significant excess in the pn spectrum below ∼1.5 keV. This excess consisted of a "Gaussian-like" component centred at ∼1 keV. This feature has been previously modelled in a number of sources either as an emission line or as an edge, and its nature is unclear (e.g., Sidoli et al. 2001; Boirin & Parmar 2003; Boirin et al. 2004, 2005). If the feature has an astrophysical origin, its energy is consistent with Ne X or a blend of Fe XX-Fe XXIV emission. When the feature is edge-like, its energy is consistent with O VIII. We therefore fitted such a feature with a Gaussian component or with an edge whenever present, and discuss its origin in Sect. 5. We fitted the excess at ∼6−7 keV with either a Gaussian or a `laor` component (see below). Finally, we added two Gaussian absorption/emission features at ∼1.84 keV and ∼2.28 keV. Such features probably stem from an incorrect modelling of the Si and Au absorption in the CCD detectors by the EPIC pn calibration, so are not discussed further.

Summarising, our final model consisted of disc blackbody and blackbody components, one Gaussian emission feature at ∼1 keV (or absorption edge at ∼0.87 keV), and one emission feature at ∼6.5 keV (modelled with Gaussian or `laor`), both modified by photo-electric absorption from neutral material, and two narrow Gaussian features at ∼1.84 and ∼2.28 keV to account for the calibration deficiencies at these energies (Models 1a and 2a, see Table 2).

The fits with Model 1a were acceptable for fifteen out of the nineteen observations for which we extracted a spectrum,
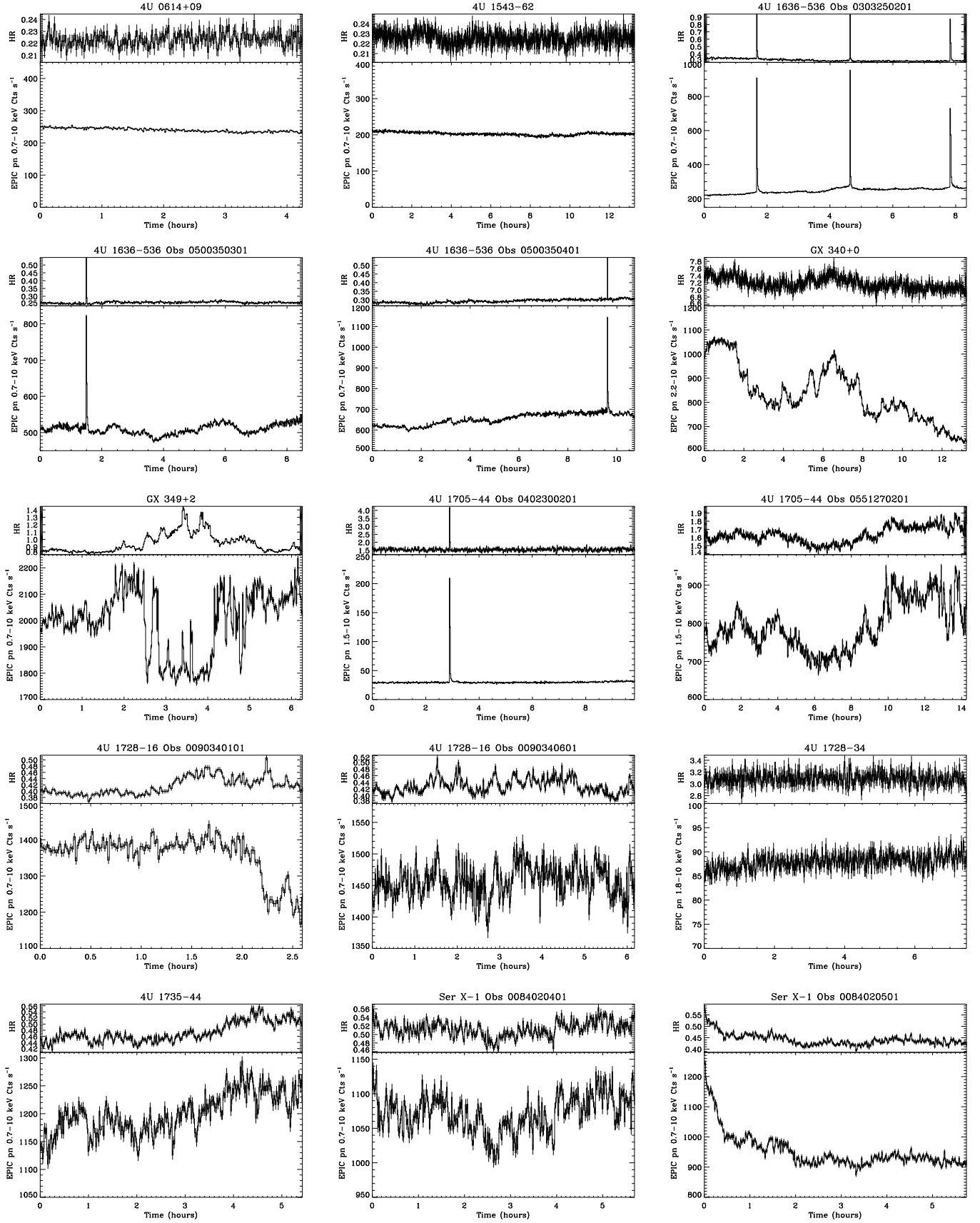
Fig. 2. EPIC pn light curves and hardness ratios (HR) for all the observations of our sample with a binning of 64 s. Time is shown in hours since the beginning of the observation. The hardness ratio is obtained dividing the bins in the 3−10 keV energy range by those in the 0.7−3 keV energy range, except for 4U 1705−44, 4U 1728−34, and GX 340+0, for which the soft band is 1.5−3 keV, 1.8−3 keV, and 2.2−3 keV, respectively.
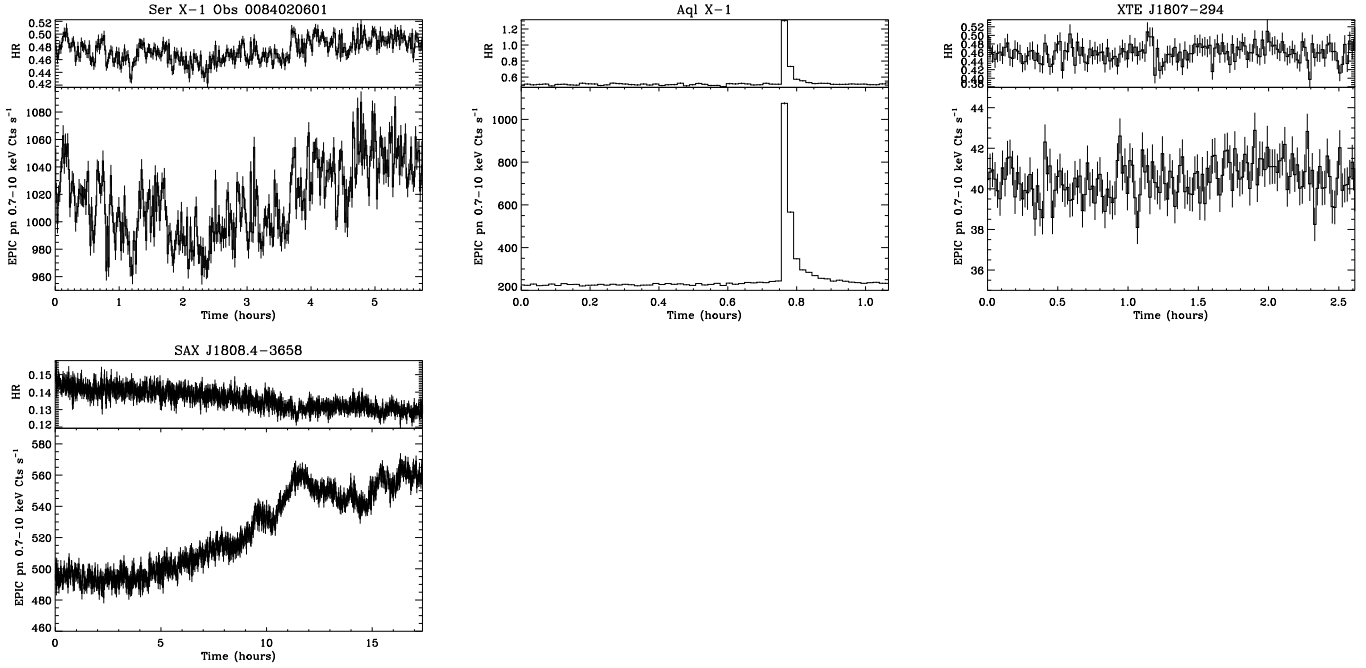
Fig. 2. continued.

Table 2. Description of the models (M) used to fit the spectra in XSPEC notation.

M	Description
1a	tbabs*(diskbb+bbodyrad+gau$_1$/edge$_1$+gau$_2$)+gau$_3$+gau$_4$
1b	tbabs*(diskbb+po+gau$_1$/edge$_1$+gau$_2$)+gau$_3$+gau$_4$
1c	tbabs*(bbodyrad+po+gau$_1$/edge$_1$+gau$_2$)+gau$_3$+gau$_4$
1d	tbabs*(diskbb+bbodyrad+po+gau$_1$/edge$_1$+gau$_2$) +gau$_3$+gau$_4$
2a	tbabs*(diskbb+bbodyrad+gau$_1$/edge$_1$+laor)+gau$_3$+gau$_4$
2b	tbabs*(diskbb+po+gau$_1$/edge$_1$+laor)+gau$_3$+gau$_4$
2c	tbabs*(bbodyrad+po+gau$_1$/edge$_1$+laor)+gau$_3$+gau$_4$
2d	tbabs*(diskbb+bbodyrad+po+gau$_1$/edge$_1$+laor) +gau$_3$+gau$_4$

with χ^2_ν between 0.7 and 1.2 for a number of degrees of freedom (d.o.f.) between 161 and 221. The parameters of the best fit with this model are given in Table 3, and the residuals of the fits are shown in Fig. C.1 (see Appendix C).

Substituting the blackbody or disc blackbody components in Model 1a by a power law component resulted in fits with similar or worse χ^2_ν for all the observations shown in Table 3 (see Table 6). Substituting the blackbody component by a cutoff power law in Model 1a resulted in fits with similar χ^2_ν. This is expected, since the blackbody in Model 1a accounts for the emission of the boundary layer and could therefore be equally well fitted by a cutoff power law or a `comptt` component, representing saturated Comptonisation. Finally, substituting the disc blackbody component by a cutoff power law in Model 1a resulted in fits with similar χ^2_ν, but with unrealistic values for the index and the cutoff energy of the cutoff power law component. For example, for the bright source GX 349+2, we obtained an index of -0.2 ± 0.4 and an energy for the cutoff of $1.0^{+0.3}_{-0.2}$ keV. Similarly, for the dim source 4U 1728−34, we obtained an energy for the cutoff of 0.51 ± 0.02 keV, and the index was unconstrained. Fixing the index of the cutoff power law to a more

realistic value of 1 (Hasinger et al. 1990) yielded fits with significantly worse χ^2_ν.

We compared the χ^2_ν for the different continua before adding the emission line at ∼6.5 keV to avoid the *EW* of the line being affected by the possible deficiencies of the fit to the continuum. Whenever two different continua yielded a similar χ^2_ν before including the Fe line, e.g. using a disc blackbody in combination with a blackbody or cutoff power law components, the breadth of the line was similar in both fits.

For one of the remaining four observations, corresponding to XTE J1807−294, we had already obtained an acceptable χ^2_ν of 1.20 for 224 d.o.f. when fitting the continuum with Model 1a. However, a better fit was obtained substituting the blackbody or disc blackbody components by a power law (Models 1b or 1c, see Table 2), with a final χ^2_ν of 1.00 (Model 1b) and 1.02 (Model 1c) for 224 d.o.f. None of the fits showed significant residual emission at ∼1 or ∼6.5 keV. We calculated an upper limit of 17 eV for the *EW* of a potential Fe line with an energy of 6.6 keV and a width of 0.3 keV in this observation. For the other AMXP in our sample, SAX J1808.4−3658, fitting the spectrum with Models 1a or 1b gave significantly worse results (χ^2_ν of 20.7 and 2.2 for 224 d.o.f., respectively) than with Model 1c (χ^2_ν of 1.1 for 224 d.o.f.). Since XTE J1807−294 was equally well fitted with Models 1b and 1c and SAX J1808.4−3658 was best-fit with Model 1c, we chose the latter to model both sources, thus allowing a better comparison of the parameters. For SAX J1808.4−3658, we show two fits, corresponding to 2 different spectra: one extracted using the full PSF and one after removal of the 2 central columns of the PSF (marked with ** in Tables 4, 5). The reason is that it was difficult to decide based on the `epatplot` whether the original spectrum had some residual pile-up. The second spectrum (**) was completely free of pile-up. We show the parameters of the best fit for XTE J1807−294 and SAX J1808.4−3658 in Table 4.

Similarly, for 4U 0614+09, we obtained a better χ^2_ν of 1.19 (220) with Model 1c, compared to 2.25 (220) with Model 1a

Table 3. Best fits to the EPIC pn spectra for all the observations (except for XTE J1807−294, SAX J1808.4−3658, 4U 0614+09 and 4U 1636−536 Obs 0303250201, which are shown in Table 4) using Model 1a (tbabs* (bbrad+dbb+gau$_1$/edge$_1$+gau$_2$)+gau$_3$+gau$_4$) or Model 2a (tbabs* (bbrad+dbb+gau$_1$/edge$_1$+1aor)+gau$_3$+gau$_4$).

Target	Observation	tbabs N_H^{abs} (10^{21} cm^{-2})	dbb kT_{dbb} (keV)	k_{dbb}	bbrad kT_{bb} (keV)	k_{bb}	gau$_1$ E_{gau} (keV)	σ (keV)	k_{gau}	EW (eV)	F_9	χ^2_ν (d.o.f.)	Model
4U 1636−536	0500350301	2.38 ± 0.04	0.80 ± 0.01	177 ± 9	1.86 ± 0.02	8.24 ± 0.3	1.0 (f)	0.31 ± 0.02	252 ± 30	63 ± 7.5	1.34	0.71 (218)	1a
		2.38 ± 0.03	0.80 ± 0.01	177 ± 8	1.86 ± 0.02	8.2 ± 0.3	1.0 (f)	0.31 ± 0.02	253^{+32}_{-16}	62^{+8}_{-4}	1.34	0.70 (217)	2a
	0500350401	2.49 ± 0.04	0.84 ± 0.01	185^{+5}_{-4}	1.80 ± 0.02	12.3 ± 0.5	1.06 ± 0.06	$0.23^{+0.17}_{-0.08}$	159^{+450}_{-55}	35^{+98}_{-30}	1.82	0.72 (217)	1a
		$2.50^{+0.09}_{-0.04}$	0.83 ± 0.01	196 ± 7	1.80 ± 0.01	12.7 ± 0.4	$1.08^{+0.05}_{-0.14}$	$0.20^{+0.08}_{-0.05}$	123^{+135}_{-38}	27^{+30}_{-8}	1.82	0.80 (215)	2a
GX 340+0	0505950101	65.0 ± 1.9	$0.96^{+0.07}_{-0.05}$	757^{+235}_{-208}	1.64 ± 0.03	147^{+13}_{-10}	—	—	—	—	15.3	0.86 (163)	1a
		$65.2^{+1.8}_{-0.7}$	0.95 ± 0.05	787^{+228}_{-184}	1.64 ± 0.02	150^{+13}_{-10}	—	—	—	—	15.3	0.88 (161)	2a
GX 349+2	0506110101	7.0 ± 0.1	0.92 ± 0.03	465^{+59}_{-55}	1.57 ± 0.02	169 ± 10	1.06 ± 0.02	0.09 ± 0.02	517^{+131}_{-101}	31^{+8}_{-6}	12.1	1.15 (216)	1a
		7.0 ± 0.1	0.93 ± 0.04	443 ± 56	1.58 ± 0.02	164^{+8}_{-12}	1.06 ± 0.02	0.09 ± 0.02	519^{+126}_{-101}	31 ± 7	12.1	1.14 (214)	2a
4U 1705−44	0402300201	$15.8^{+0.2}_{-0.4}$	1.31 ± 0.06	3.6 ± 0.6	2.76 ± 0.2	0.37 ± 0.08	—	—	—	—	0.25	0.99 (186)	1a
		15.8 ± 0.3	$1.30^{+0.06}_{-0.03}$	$3.7^{+0.6}_{-0.3}$	2.74 ± 0.2	$0.38^{+0.05}_{-0.07}$	—	—	—	—	0.25	1.01 (184)	2a
	0551270201	15.0 ± 0.5	$0.95^{+0.05}_{-0.07}$	231 ± 52	1.61 ± 0.03	79^{+6}_{-8}	—	—	—	—	6.5	1.07 (187)	1a
		$14.7^{+0.5}_{-0.3}$	1.01 ± 0.06	184^{+51}_{-32}	1.64 ± 0.03	71 ± 6	—	—	—	—	6.5	1.03 (185)	2a
GX 9+9	0090340101	1.50 ± 0.07	1.02 ± 0.06	148^{+31}_{-26}	1.76 ± 0.06	36 ± 6	1.0 (f)	0.20 ± 0.07	213 ± 100	29 ± 14	4.55	0.99 (220)	1a/2a
	0090340601	1.48 ± 0.05	0.96 ± 0.03	187 ± 17	1.71 ± 0.02	49 ± 3	$1.05^{+0.03}_{-0.05}$	$0.08^{+0.08}_{-0.03}$	76^{+71}_{-23}	11^{+10}_{-3}	5.03	0.89 (219)	1a/2a
4U 1728−34	0149810101	27.0 ± 0.5	1.9 ± 0.3	$3.5^{+1.5}_{-1.9}$	$3.8^{+8.4}_{-1.1}$	$0.3^{+0.9}_{-0.2}$	—	—	—	—	0.97	1.02 (177)	1a
		27.6 ± 0.4	$1.48^{+0.14}_{-0.10}$	$7.4^{+1.1}_{-0.6}$	$2.56^{+0.11}_{-0.06}$	1.9 ± 0.2	—	—	—	—	0.97	1.07 (175)	2a
4U 1735−44	0090340201	$1.85^{+0.10}_{-0.05}$	0.93 ± 0.02	171^{+15}_{-17}	1.89 ± 0.02	33 ± 2	$1.04^{+0.02}_{-0.05}$	$0.15^{+0.06}_{-0.03}$	218^{+142}_{-57}	36^{+23}_{-9}	4.60	0.68 (216)	1a
		$1.85^{+0.08}_{-0.05}$	0.93 ± 0.02	172^{+17}_{-11}	1.89 ± 0.02	33 ± 1	$1.04^{+0.03}_{-0.05}$	0.15 ± 0.04	220^{+91}_{-61}	36^{+15}_{-10}	4.60	0.78 (214)	2a
Ser X−1	0084020401	$3.67^{+0.08}_{-0.08}$	0.86 ± 0.02	292 ± 24	1.60 ± 0.02	53 ± 3	$1.06^{+0.02}_{-0.04}$	$0.13^{+0.04}_{-0.04}$	216^{+105}_{-45}	27^{+13}_{-6}	4.41	0.98 (216)	1a
		$3.66^{+0.08}_{-0.04}$	0.87 ± 0.01	284^{+12}_{-21}	1.61 ± 0.01	52 ± 2	1.06 ± 0.03	$0.13^{+0.03}_{-0.04}$	221^{+100}_{-38}	28^{+13}_{-5}	4.41	0.97 (214)	2a
	0084020501	$3.60^{+0.11}_{-0.07}$	0.91 ± 0.02	233 ± 18	1.64 ± 0.03	33.7 ± 2.6	$1.07^{+0.03}_{-0.02}$	$0.14^{+0.07}_{-0.03}$	201^{+187}_{-46}	27^{+22}_{-2}	3.58	0.93 (216)	1a
		$3.59^{+0.07}_{-0.05}$	0.92 ± 0.02	230^{+7}_{-14}	1.65 ± 0.03	$33.0^{+2.6}_{-3.1}$	$1.07^{+0.02}_{-0.07}$	$0.14^{+0.06}_{-0.03}$	201^{+155}_{-43}	27^{+21}_{-6}	3.58	0.92 (214)	2a
	0084020601	$3.68^{+0.08}_{-0.10}$	0.87 ± 0.02	277^{+25}_{-23}	1.61 ± 0.02	44.2 ± 3.0	$1.06^{+0.03}_{-0.03}$	$0.14^{+0.05}_{-0.03}$	203^{+134}_{-55}	26^{+17}_{-7}	3.97	1.04 (216)	1a
		$3.69^{+0.08}_{-0.05}$	0.87 ± 0.02	277^{+21}_{-13}	1.61 ± 0.02	$44.0^{+2.5}_{-1.6}$	$1.06^{+0.03}_{-0.05}$	$0.14^{+0.05}_{-0.03}$	201^{+122}_{-46}	25^{+15}_{-6}	3.97	1.04 (214)	2a
Aql X−1	0303220201	$2.37^{+0.23}_{-0.09}$	1.10 ± 0.03	25 ± 3	$2.25^{+0.07}_{-0.05}$	3.4 ± 0.4	$1.01^{+0.03}_{-0.09}$	$0.15^{+0.06}_{-0.03}$	76^{+75}_{-20}	51^{+51}_{-14}	1.01	0.97 (221)	1a/2a

Target	Observation	tbabs N_H^{abs} (10^{21} cm^{-2})	dbb kT_{dbb} (keV)	k_{dbb}	bbrad kT_{bb} (keV)	k_{bb}	edge$_1$ E_{edge} (keV)	τ			F_9	χ^2_ν (d.o.f.)	Model
4U 1543−62	0061140201	0.71 ± 0.04	0.640 ± 0.005	140 ± 5	1.539 ± 0.006	$6.99^{+0.14}_{-0.16}$	$0.842^{+0.008}_{-0.008}$	0.20 ± 0.02	—	—	0.47	0.97 (217)	1a
		0.70 ± 0.04	$0.642^{+0.005}_{-0.008}$	137 ± 5	1.541 ± 0.006	6.94 ± 0.12	$0.841^{+0.008}_{-0.005}$	0.20 ± 0.02	—	—	0.47	0.96 (215)	2a

Notes. gau$_1$/edge$_1$ models the emission feature at ~1 keV with a Gaussian component or an edge, respectively. kT_{bb}, and kT_{dbb} are the temperatures of the blackbody and disc blackbody components respectively. k_{bb}, k_{dbb}, and k_{gau} are the normalisations of the blackbody, disc blackbody, and gau$_1$ components in units of $(R_{in}/D_{10})^2$, $(R_{in}/D_{10})^2$ cosθ and 10^{-4} ph cm^{-2} s^{-1} respectively. E_{gau} and σ represent the energy and width of the Gaussian feature. E_{edge} is the edge energy and τ its optical depth. F_9 is the unabsorbed 2–10 keV total flux in units of 10^{-9} erg cm^{-2} s^{-1}. We show two rows per observation corresponding to fits with Models 1a and 2a, except for observations for which no significant emission was found at the 6 keV range, since in this case Models 1a and 2a are the same model, namely 'tbabs* (bbrad+dbb+gau$_1$/edge$_1$)+gau$_3$+gau$_4$. We do not show the values of gau$_3$ and gau$_4$, since they are fixed calibration features. The parametres of gau$_2$ and 1aor/1aor components are shown in Table 5. The spectrum energy range is 1.5–10, 1.8–10 and 2.2–10 keV for 4U 1705−44, 4U 1728−34 and GX 340+0, respectively, and 0.7–10 keV otherwise (see text).

Table 4. Best fits to the 0.7–10 keV EPIC pn spectra for XTE J1807−294, SAX J1808.4−3658 and 4U 0614+09 using Model 1c (tbabs*(bbrad+po+gau₁+gau₂)+gau₃+gau₄) or Model 2c (tbabs*(bbrad+po+gau₁+laor)+gau₃+gau₄) and) to the 0.7–10 keV EPIC pn spectra for 4U 1636−536 Obs 0303250201 with Model 1d (tbabs*(bbrad+dbb+po+gau₁+gau₂)+gau₃+gau₄) or Model 2d (tbabs*(bbrad+dbb+po+gau₁+laor)+gau₃+gau₄).

Target	Observation	tbabs N_H^{abs} (10^{21} cm^{-2})	bbrad kT_{bb} (keV)	k_{bb}	po Γ	k_{pl}	gau₁ E_{gau} (keV)	σ (keV)	k_{gau}	EW (eV)	F_9	χ^2_ν(d.o.f.)	M
XTE J1807−294	0157960101	5.27 ± 0.14	0.69 ± 0.02	12 ± 2	1.79 ± 0.03	0.043 ± 0.002	–	–	–	–	0.17	1.02 (224)	1c/2c
SAX J1808.4−3658	0560180601	1.46 ± 0.04	2.21 ± 0.03	1.12 ± 0.08	2.55 ± 0.01	0.550 ± 0.006	–	–	–	–	0.83	0.75 (220)	1c
		1.43 ± 0.04	2.26 ± 0.05	$1.01^{+0.13}_{-0.05}$	2.54 ± 0.02	0.546 ± 0.006	–	–	–	–	0.83	0.71 (218)	2c
SAX J1808.4−3658	0560180601**	1.52 ± 0.05	2.08 ± 0.03	1.4 ± 0.1	2.59 ± 0.02	0.540 ± 0.007	–	–	–	–	0.80	0.86 (220)	1c
		1.53 ± 0.05	2.08 ± 0.03	$1.43^{+0.05}_{-0.12}$	2.59 ± 0.02	0.542 ± 0.007	–	–	–	–	0.80	0.84 (218)	2c

edge₁: E_{edge} (keV), τ

Target	Observation	tbabs N_H^{abs} (10^{21} cm^{-2})	bbrad kT_{bb} (keV)	k_{bb}	po Γ	k_{pl}	edge₁ E_{edge} (keV)	τ	k_{gau}	EW (eV)	F_9	χ^2_ν(d.o.f.)	M
4U 0614+09	0111040101	1.89 ± 0.07	$0.64^{+0.07}_{-0.05}$	17^{+10}_{-7}	2.16 ± 0.02	0.275 ± 0.008	0.856 ± 0.007	0.20 ± 0.02	–	–	0.58	0.82 (217)	1c
		1.87 ± 0.07	0.61 ± 0.04	21^{+10}_{-7}	2.15 ± 0.02	0.272 ± 0.008	0.856 ± 0.007	0.20 ± 0.02	–	–	0.58	0.84 (215)	2c

gau₁: E_{gau} (keV), σ (keV), k_{gau}, EW (eV)

Target	Observation	tbabs N_H^{abs} (10^{21} cm^{-2})	bbrad/dbb kT_{dbb} (keV)	k_{dbb}	po Γ	k_{pl}	gau₁ E_{gau} (keV)	σ (keV)	k_{gau}	EW (eV)	F_9	χ^2_ν(d.o.f.)	M
4U 1636−536	0303250201	2.77 ± 0.03	$1.78^{+0.45}_{-0.18}$	$1.0^{+0.5}_{-0.3}$	1.86 ± 0.02	$0.204^{+0.001}_{-0.002}$	1.02 ± 0.03	$0.22^{+0.05}_{-0.03}$	83 ± 3	38 ± 1	0.76	0.76 (216)	1d
		$2.61^{+0.02}_{-0.05}$	$1.74^{+0.03}_{-0.08}$	$1.29^{+0.25}_{-0.27}$	$1.820^{+0.004}_{-0.022}$	$0.187^{+0.005}_{-0.004}$	$0.88^{+0.02}_{-0.03}$	$0.314^{+0.025}_{-0.040}$	183^{+35}_{-24}	69^{+13}_{-9}	0.76	0.78 (214)	2d
		0.42 ± 0.04	63^{+32}_{-29}										1d
		$0.58^{+0.2}_{-0.02}$	$29.9^{+4.0}_{-5.5}$										2d

Notes. The parameters of the models are the same as in Table 3, except Γ and k_{pl}, index and normalisation of the power law component, the latter is in units of [ph keV^{-1} cm^{-2} s^{-1}]. We show one row for each observation whenever no line was found at the 6 keV range, since in this case the two models 1c and 2c or 1d and 2d are the same model. For SAX J1808.4−3658 we show results for two spectra, which only differ in the pile-up treatment (see text).

Table 5. Parameters of the Gaussian (Models 1a, 1b, 1c, and 1d) and 1aor (Models 2a, 2b, 2c and 2d) components used to model the Fe emission at ∼6 keV.

Target	Observation	$E_{\rm gau}$ (keV)	σ (keV)	$k_{\rm gau}$	EW (eV)	$E_{\rm laor}$ (keV)	β	$r_{\rm in}$	i (°)	$k_{\rm laor}$	EW (eV)
		gau₂				1aor					
4U 0614+09	0111040101	6.79 ± 0.16	$0.94^{+0.3}_{-0.2}$	8^{+5}_{-3}	185^{+116}_{-69}	6.50 ± 0.10	2.1 ± 0.3	$4.0^{+5.2}_{-3.9*}$	70^{+0*}_{-7}	7^{+1}_{-2}	160^{+23}_{-46}
4U 1543−62	0061140201	$6.77^{+0.14}_{-0.16}$	0.33 ± 0.13	$0.97^{+0.44}_{-0.39}$	23^{+11}_{-9}	$6.56^{+0.41*}_{-0.10}$	$3.6^{+1.4*}_{-2.1}$	64^{+37}_{-54}	63^{+7*}_{-39}	1.21 ± 0.35	32 ± 9
4U 1636−536	0303250201	6.78 ± 0.01	1.15 ± 0.17	14.6 ± 9	210 ± 129	$6.40^{+0.12}_{-0*}$	2.3 ± 0.2	<6.25	70^{+0*}_{-1}	9 ± 1	130 ± 14
	0500350301	$6.97^{+0*}_{-0.16}$	0.6 ± 0.3	3 ± 2	28 ± 19	6.97 (f)	$2.2^{+2.8*}_{-1.1}$	<64	50^{+20*}_{-8}	$3.5^{+3.3}_{-1.7}$	36^{+34}_{-16}
	0500350401	$6.97^{+0.00*}_{-0.08}$	$0.94^{+0.37}_{-0.26}$	$8.3^{+2.0}_{-2.4}$	59^{+15}_{-17}	$6.95^{+0.02*}_{-0.10}$	4.8 (f)	205.8 (f)	14 (f)	0.9 ± 0.5	6 ± 3
GX 340+0	0505950101	6.72 ± 0.06	$0.17^{+0.14}_{-0.08}$	$22.0^{+11.8}_{-7.5}$	17^{+9}_{-6}	$6.82^{+0.07}_{-0.13}$	2.56 (f)	>16	<34	$19.7^{+5.6}_{-5.4}$	15 ± 5
GX 349+2	0506110101	6.72 ± 0.06	$0.32^{+0.11}_{-0.07}$	96^{+26}_{-18}	82^{+22}_{-15}	$6.94^{+0.03*}_{-0.22}$	$3.1^{+0.7}_{-1.0}$	11^{+7}_{-5}	17 ± 9	104^{+21}_{-15}	96^{+20}_{-14}
4U 1705−44	0402300201	6.53 ± 0.07	$0.34^{+0.05}_{-0.07}$	1.4 ± 0.4	57 ± 16	6.51 ± 0.08	<3.1	<110	45 ± 12	1.4 ± 0.4	58 ± 16
	0551270201	6.56 ± 0.05	$0.44^{+0.05}_{-0.07}$	61^{+15}_{-5}	92^{+23}_{-8}	$6.45^{+0.05}_{-0.05*}$	$1.8^{+0.1}_{-0.2}$	<9.1	65^{+5*}_{-5}	83^{+6}_{-13}	135^{+10}_{-21}
Ser X−1	0084020401	6.61 ± 0.05	$0.22^{+0.08}_{-0.05}$	22^{+6}_{-5}	52^{+14}_{-11}	$6.79^{+0.1}_{-0.2}$	$2.84^{+0.9}_{-0.8}$	13.3^{+19}_{-7}	<33	25.2 ± 4.8	63 ± 12
	0084020501	6.58 ± 0.07	0.25 ± 0.08	$15.7^{+4.5}_{-3.9}$	50^{+14}_{-12}	6.6 ± 0.1	2.03 (f)	11.15 (f)	28 ± 9	17.5 ± 4	59 ± 13.5
	0084020601	$6.59^{+0.07}_{-0.09}$	$0.27^{+0.14}_{-0.10}$	$18.7^{+7.7}_{-5.6}$	51^{+21}_{-15}	$6.73^{+0.24*}_{-0.23}$	$2.6^{+2.4*}_{-1.1}$	11^{+26}_{-10*}	<25	$19.4^{+6.2}_{-5.8}$	57 ± 18
4U 1728−34	0149810101	6.72 ± 0.10	$0.98^{+0.19}_{-0.16}$	21^{+12}_{-9}	189^{+108}_{-81}	$6.53^{+0.11}_{-0.06}$	2.6 ± 0.4	20^{+5}_{-7}	70^{+0*}_{-16}	$7.7^{+1.6}_{-1.2}$	80^{+22}_{-15}
4U 1735−44	0090340201	6.74 ± 0.10	0.38 ± 0.11	22 ± 7	46 ± 14	$6.73^{+0.09}_{-0.18}$	<2.94	5.41 (f)	44^{+16}_{-19}	20 ± 6	43 ± 13
SAX J1808.4−3658	0560180601	$6.94^{+0.03*}_{-0.12}$	$0.26^{+0.12}_{-0.08}$	$1.5^{+0.6}_{-0.4}$	23^{+9}_{-7}	$6.50^{+0.42}_{-0.24}$	$3^{+2*}_{-0.8}$	$6.3^{+26}_{-5.1*}$	46^{+7}_{-13}	$3.1^{+1.2}_{-1.0}$	51^{+20}_{-16}
	0560180601**	6.77 ± 0.13	$0.39^{+0.14}_{-0.11}$	1.9 ± 0.7	30 ± 11	$6.96^{+0.01*}_{-0.24}$	$5.0^{+0*}_{-2.6}$	33^{+60}_{-18}	26^{+13}_{-4}	1.8 ± 0.6	31 ± 10

Notes. $E_{\rm gau}$ and σ represent the energy and width of the Gaussian feature. The parameters of the 1aor component $E_{\rm laor}$, β, $r_{\rm in}$, i and $k_{\rm laor}$ account for energy, emissivity index, inner radius (in units of $r_{\rm g}$), inclination and normalisation. β is constrained to be <5. The inner radius is constrained to be $>1.235\ r_{\rm g}\ (GM/c^2)$. The inclination is constrained to be $<70°$, since none of the sources is a known dipper or eclipsing system. The outer radius has been fixed to $400\ r_{\rm g}$ for all sources, since it is not well constrained. The normalisation is in units of $(10^{-4}\ {\rm ph\ cm^{-2}\ s^{-1}})$ for both components. Parameters that are completely unconstrained when the errors are calculated have been fixed at their best value and are indicated in the table with "(f)". A star (∗) means that the error has reached the maximum or minimum allowed value of the parameter. For SAX J1808.4−3658 we show results for two spectra, which only differ in the pile-up treatment (see text).

and 1.21 (220) with Model 1b. We show the parameters of the best fit for this source in Table 4.

Finally, for Obs 0303250201 of 4U 1636−536 we needed three continuum components, blackbody, disc blackbody, and power law, in order to obtain an acceptable χ_ν^2. Fits of this observation with a simultaneous RXTE observation also require three components and show a power law extending well above 10 keV (Pandel et al. 2008). We show the parameters of the best fit for this observation in Table 4.

Next, we examined the asymmetry of the line and evaluated to what extent the Fe emission was better approximated by a model including relativistic effects. For this, we substituted the second Gaussian component at ~6.5 keV (gau$_2$) in Models 1a, 1b, and 1c by a `laor` component and re-fitted all the spectra with the new models (Models 2a, 2b, and 2c, see Table 2). We show the parameters of the best fit with these models in Tables 3, 4 and the residuals of the fits in Fig. C.1. The fits with Models 2a, 2b, and 2c were again acceptable, with χ_ν^2 between 0.8 and 1.2 for a number of d.o.f. between 161 and 221, i.e. similar to the χ_ν^2 obtained when a simple Gaussian model was used to fit the lines.

We found that fits to continua different to the one selected that yielded significantly higher values of χ_ν^2 had a clear influence on the line breadth for all the sources analysed in this work.

Narrow absorption features were not visible in any of the spectra, as expected for sources that are not at high inclination. Similarly, adding an absorption edge to the best-fit models shown in Table 3 did not significantly improve the goodness of the fits for any source with the exception of GX 349+2. For this source, the χ_ν^2 improved from 1.15 (216) to 1.07 (214) after adding an edge at ~9.2 ± 0.1 keV, which we attribute to absorption from Fe XXVI. The parameters of the Fe line did not change after including this additional edge. This edge was previously detected in a BeppoSAX observation of the source (Iaria et al. 2004).

For sources with significant emission at ~6.5 keV, the parameters of the continuum did not change significantly when fitting the former with a Gaussian or a `laor` component, except for 4U 1728−34. Previous analyses of this source based on *Chandra* and RXTE or BeppoSAX data (D'Aì et al. 2006) have shown equally good fits when modelling the emission at ~6.5 keV with a broad line or with two absorption edges. Therefore, we regard the *XMM-Newton* fits from 4U 1728−34 in this work with caution and discuss them in the framework of the general properties of the Fe lines in the following sections. Figure 3 shows the ratio between the data and the best-fit model at the Fe line energy band for all the sources with significant emission when the Fe line is not included.

4. Properties of the sample

4.1. Fe line emission

Examination of the spectral fits (Tables 3 to 5 and Figs. C.1−C.2) shows that we are able to successfully model the emission in the Fe K band with a simple Gaussian component. Fits of the excess in the Fe K band with the more complicated `laor` component do not improve the goodness of the fit significantly for any of the observations presented here (see Table 6).

Considering the whole sample, the Fe line has a weighted average energy of 6.67 ± 0.02 keV, a width of 0.33 ± 0.02 keV, and an *EW* of 42 ± 3 eV. The statistical distribution of these values is shown in Fig. 4. The width and the *EW* have a well-defined "Gaussian-like" distribution around the weighted average value.

The outliers of the histograms in Fig. 4 have values with large errors, so they do not contribute to the weighted average significantly. The energy distribution peaks at ~6.7 keV, in agreement with the value of the weighted average. This is consistent with emission from Fe XXV. Clearly, the distribution has values consistent with emission from highly ionised species of Fe, from Fe XXII to Fe XXVI, and it never shows a value consistent with neutral Fe.

To find out the reason for the large errors in the lines with an *EW* above 30 eV, we plotted the *EW* of the lines as a function of the total number of counts in the spectrum (see Fig. 5). The lines that show large errors are not associated to the spectra with fewer counts, indicating that the detection of the lines within our sample is not limited by statistics. Therefore, we examined in detail the three cases for which the errors on the parameters of the line are very large (corresponding to 4U 0614+09, 4U 1636−536 Obs 0303250201, and 4U 1728−34) to determine the reason for such large errors. As indicated in Sect. 3.2, fits to 4U 1728−34 spectra of *Chandra* and RXTE or BeppoSAX (D'Aì et al. 2006) show equally good fits when modelling the emission at ~6.5 keV with a broad line or with two absorption edges. Including one edge in the *XMM-Newton* spectrum at 7.6 keV and no Fe line yields a χ_ν^2 of 1.32 (178). Although the χ_ν^2 is higher than when including the Fe line, the residuals at the Fe band are reduced considerably. The fits to the *XMM-Newton* spectrum have significantly different continuum parameters when fitting the residuals at the Fe band with Models 1a or 1b (see Table 3), in contrast to all other observations. This indicates that after including the line, the parameters of the fit change significantly so the line fit may not be realistic. Interestingly, 4U 0614+09 and 4U 1728−34 show the lowest luminosities of the full sample. Therefore, it is plausible that such observations have a significantly different, more complex spectrum compared to higher luminosity observations. For comparison, the MOS spectra of the observation of 4U 0614+09 analysed in this work were previously fitted with an absorbed power law and an emission feature at 0.65 keV (Méndez et al. 2002) and did not require a line at ~6.5 keV. In the case of 4U 1636−536 Obs 0303250201, although the luminosity is higher than for other sources in our sample fitted with the "standard" Model 1a/1b, we needed three continuum components to obtain an acceptable fit. This again points to a complex spectrum. Figure 6 shows the residuals of the fit to the continuum before including the Fe line for the three observations discussed. The residuals at the Fe energy band are very different than those shown in Fig. 3, indicating that the lines fitted for these observations may not be realistic and that such fits may need, e.g., the inclusion of absorption edges. For these reasons we regard the properties of these lines with caution.

It is interesting to compare the properties of the Fe Kα line with general properties of the sources such as luminosity or temperatures of the blackbody and disc blackbody components, with the aim of constraining the origin of the line emission region. For example, we may expect a correlation between the source accretion rate and the breadth of the line, if the latter is caused by relativistic effects. Figure 7 shows the properties of the Fe Kα line (width and *EW*) as a function of the luminosity calculated in Table 7.

We do not find any clear correlation between the energy centroid, the width, or the *EW* of the Fe line with the source luminosity (see Fig. 7). The source luminosities range over 2 orders of magnitude, covering the full range of Eddington ratios from 0.003 to 1.26, while the line centroid, width, and *EW* do not show any systematic trend. Similary, we do not find any clear
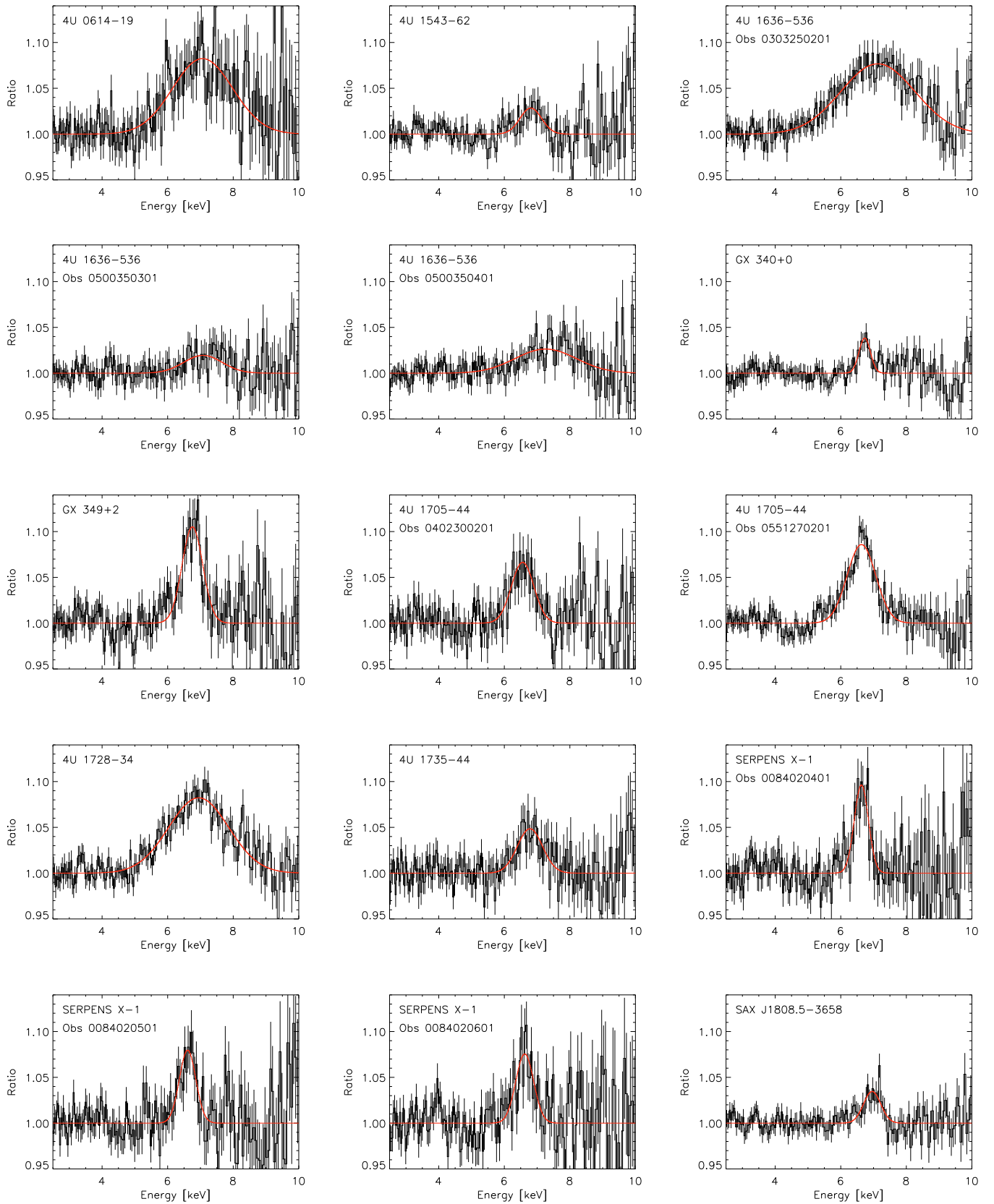
Fig. 3. Ratio of the data to the continuum model for all the neutron-star LMXBs analysed in this work for which significant Fe K emission is detected.

Table 6. χ_ν^2 of spectral fits to (a) `diskbb+bbodyrad`, (b) `diskbb+po` and (c) `bbodyrad+po` components before inclusion of the Fe line component.

Source	Observation ID	χ_ν^2				
		a	b	c	d	e
4U 0614+09	0111040101	2.25 (220)	1.21 (220)	1.19 (220)	0.83 (217)	0.85 (216)
4U 1543−62	0061140201	1.11 (220)	12.5 (224)	4.28 (220)	0.97 (217)	0.96 (215)
4U 1636−536	0303250201	6.46 (224)	32.9 (224)	48.7 (224)	0.76 (216)	0.78 (214)
	0500350301	0.76 (220)	4.14 (220)	4.15 (220)	0.71 (217)	0.70 (215)
	0500350401	0.82 (220)	4.84 (224)	6.00 (224)	0.72 (217)	0.80 (215)
GX 340+0	0505950101	1.15 (166)	2.04 (166)	1.83 (166)	0.86 (163)	0.88 (161)
GX 349+2	0506110101	1.97 (219)	3.10 (219)	3.75 (219)	1.15 (216)	1.14 (214)
4U 1705−44	0402300201	1.34 (189)	1.56 (189)	1.58 (189)	1.01 (186)	1.03 (184)
	0551270201	3.05 (189)	5.88 (189)	4.10 (189)	1.07 (187)	1.03 (185)
GX 9+9	0090340101	0.99 (219)	3.58 (221)	1.26 (219)	–	–
	0090340601	0.91 (219)	1.27 (221)	2.13 (221)	–	–
4U 1728−34	0149810101	1.55 (180)	1.82 (180)	1.80 (180)	1.02 (177)	1.07 (175)
4U 1735−44	0090340201	0.99 (219)	1.82 (219)	1.98 (219)	0.68 (216)	0.78 (214)
Ser X−1	0084020401	1.47 (219)	2.11 (219)	3.04 (219)	0.98 (216)	0.97 (214)
	0084020501	1.24 (219)	2.07 (219)	3.04 (219)	0.93 (216)	0.92 (214)
	0084020601	1.31 (219)	1.95 (219)	2.92 (219)	1.04 (216)	1.04 (214)
Aql X−1	0303220201	0.97 (221)	1.22 (221)	1.35 (221)	–	–
XTE J1807−294	0157960101	1.20 (224)	1.00 (224)	1.02 (224)	–	–
SAX J1808.4−3658	0560180601	30.2 (224)	1.30 (223)	0.98 (223)	0.75 (220)	0.71 (218)
	056018060**	33.4 (224)	1.31 (223)	1.00 (223)	0.86 (220)	0.84 (218)

Notes. Columns (d) and (e) show the χ_ν^2 of the fit after including a Gaussian (d) and a `laor` (e) component to the best-fit model.
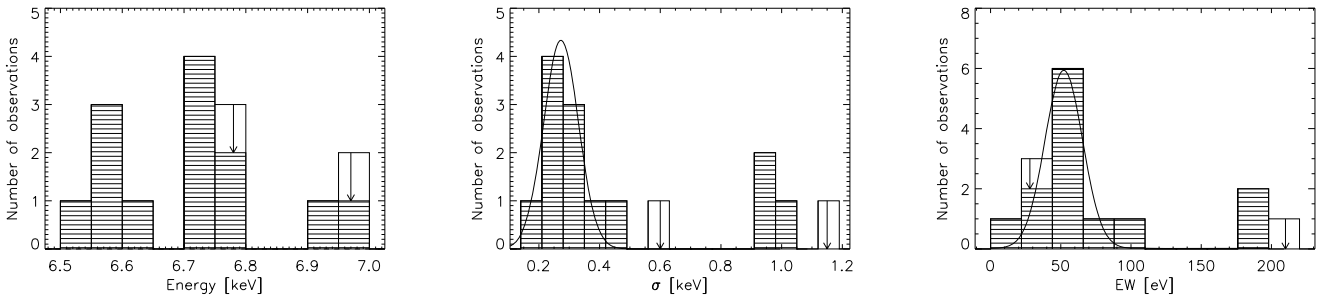
Fig. 4. Histogram of the parameters of the Fe line when fitted with a Gaussian component for the full sample considered in this work. The white rectangles marked with an arrow correspond to the lines detected below a significance of 3 σ (see Fig. 5). The width (middle panel) and the *EW* (right panel) have a well-defined "Gaussian-like" distribution around the weighted average value, while the outliers have large errors associated to their σ and *EW* values.
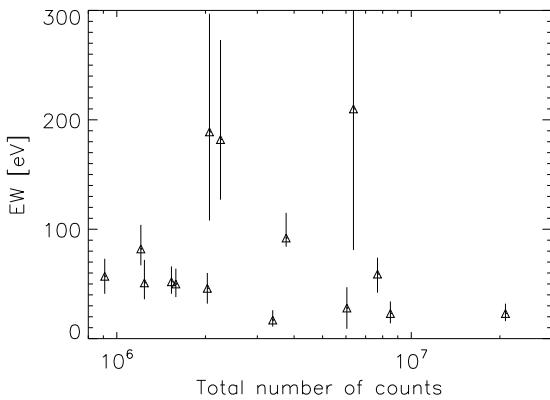
Fig. 5. *EW* of the Fe line when fitted with a Gaussian component versus the total number of counts of each spectrum.

correlation between the *EW* of the Fe line and the temperature or flux of the blackbody or disc blackbody components.

4.2. Continuum emission

We examined the continuum properties of the sample for all the sources shown in Table 3. Figure 8 shows the variation in the blackbody luminosity in the band 0.5–30 keV as a function of the total luminosity in the same band. In this figure, we excluded the two AMSP XTE J1807−294 and SAX J1808.4−3658, 4U 0614+09 and Obs 0303250201 of 4U 1636−536. The reason was that these observations were fitted with a continuum different than the standard one of blackbody and disc blackbody components and therefore indicate different properties. We further excluded the two dim observations corresponding to 4U 1705−44 (Obs 0402300201) and 4U 1728−34, since for such dim sources, Compton scattering is expected to play an important role so was not included in our model.

The blackbody luminosity is very near the value of 50% of total luminosity expected from simple energy considerations for all the sources of the sample. Interestingly, the temperature of the blackbody component, kT_{bb}, is nearly independent of the global luminosity at luminosities $\gtrsim 2 \times 10^{36}$ erg s^{-1} (Fig. 8). Ignoring the point with the highest temperature, since it has associated a significantly larger error than the other points, kT_{bb} falls by
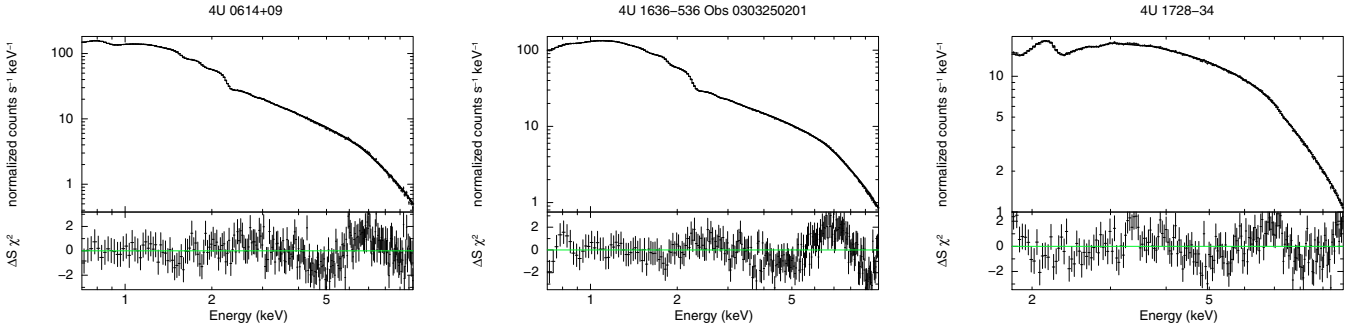
Fig. 6. Residuals in units of standard deviation from the best-fit model to the data for 4U 0614+09, 4U 1636−536 Obs 0303250201, and 4U 1728−34 before including the Fe line.
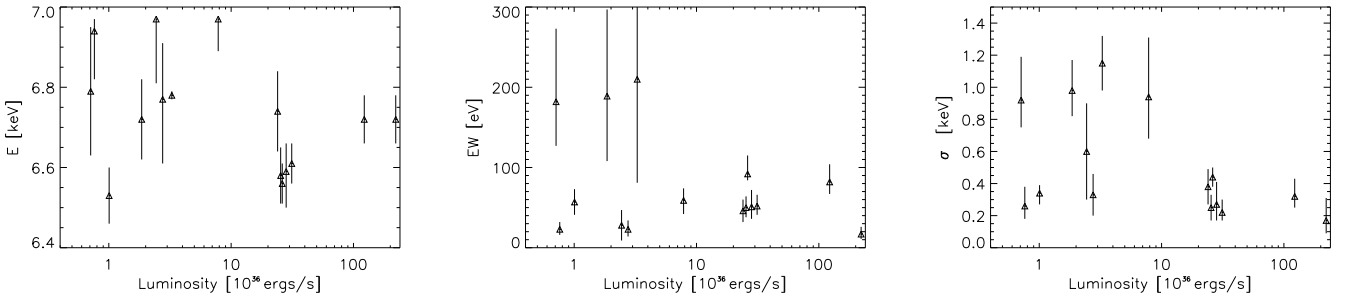

Fig. 7. Energy, *EW*, and σ of the Fe line versus luminosity of the source in the 2−10 keV energy band. The luminosity has been calculated based on the distances reported in Table 7.

Table 7. 2–10 keV luminosities in units of 10^{36} erg s^{-1} and corresponding Eddington ratios ($L_{2-10\,\mathrm{keV}}/L_{\mathrm{Eddington}}$) for all the observations in the sample.

Source	Observation ID	d [kpc]	L_{36} erg s^{-1}	R_{Edd}
4U 0614+09	0111040101	3.2 ± 0.5 (Kuulkers et al. 2009)	0.73	0.004
4U 1543−62	0061140201	7 (Wang & Chakrabarty 2004)	2.87	0.016
4U 1636−536	0303250201	6.0±0.1 (Galloway et al. 2008)	3.41	0.019
	0500350301		6.01	0.033
	0500350401		8.17	0.045
GX 340+0	0505950101	11 (Grimm et al. 2002)	230.72	1.264
GX 349+2	0506110101	9.2 (Grimm et al. 2002)	127.64	0.701
4U 1705−44	0402300201	5.8±0.2 (Galloway et al. 2008)	1.05	0.006
	0551270201		27.25	0.150
GX 9+9	0090340101	4.4 (Grimm et al. 2002)	10.98	0.060
	0090340601		12.14	0.067
4U 1728−34	0149810101	4.0 ± 0.4 (Galloway et al. 2008)	0.48	0.003
4U 1735−44	0090340201	6.6 ± 1.0 (Galloway et al. 2008)	24.97	0.137
Ser X−1	0084020401	7.7 ± 0.9 (Galloway et al. 2008)	32.59	0.179
	0084020501		26.45	0.145
	0084020601		29.33	0.161
Aql X−1	0303220201	3.9 ± 0.7 (Galloway et al. 2008)	1.91	0.010
XTE J1807−294	0157960101	8 (assumed)	1.36	0.007
SAX J1808.4−3658	0560180601	2.77 ± 0.11 (Galloway et al. 2008)	0.79	0.004

~45% while the total luminosity increases by more than two orders of magnitude and the blackbody radius by more than a factor of 40.

5. Discussion

We performed a systematic analysis of 26 *XMM-Newton* observations corresponding to all the NS LMXBs observed with EPIC pn timing mode and publicly available up until September 30, 2009 to establish the characteristics of the Fe K line emission in these objects.

In seven observations we did not detect the source significantly. For the remaining nineteen observations, we extracted one spectrum per observation. We paid special attention to the effects of pile-up and background subtraction.

5.1. Fe line emission

We detected Fe Kα line emission in 80% of the observations where the source was significantly detected. The energy of the line has values between 6.53 and 6.97 keV, consistent with
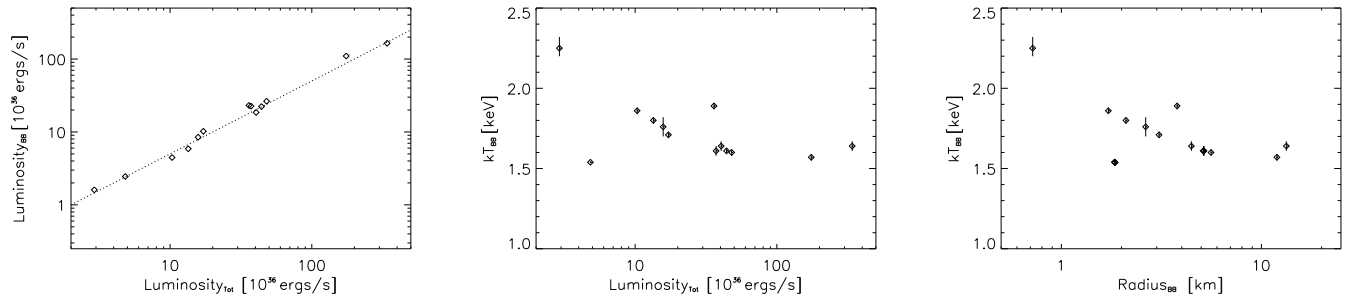
Fig. 8. *Left panel*: variation in blackbody luminosity in the band $0.5-30$ keV with total luminosity in the same band. The dashed line shows the 50% of the total luminosity. *Middle panel*: temperature of the blackbody component versus the total luminosity in the $0.5-30$ keV energy band. *Right panel*: temperature of the blackbody component versus the radius of the blackbody emission. The radius has been inferred from the normalisation of the blackbody component. See Sect. 4.2 for the observations included in this figure.

highly ionised Fe from Fe XXII to Fe XXVI. The width has values between 0.17 and 1.15 keV and the *EW* between 17 and 190 eV. Only in four cases out of the fifteen lines reported in this work did we find a width near or above 1 keV and an *EW* above 100 eV. Interestingly, there is a gap in the distributions of σ and *EW* between these high values and the rest of the sample. Lines with high values of σ or *EW* also have associated large errors. Vaughan & Uttley (2008) interpret a similar finding in the context of detection of narrow lines from AGN as the lines with large *EW*s as the most likely false detections. In the cases studied here, the lines with widths near 1 keV are also in the limit of detectability of 3σ, and the large errors most likely point to an inappropriate modelling of the continuum for 4U 0614+09, 4U 1728−34, and 4U 1636−536. Considering the whole sample, the Fe line has a weighted average energy of 6.67 ± 0.02 keV, a width (σ) of 0.33 ± 0.02 keV, and an *EW* of 42 ± 3 eV.

Recently, broad skewed Fe K emission lines from the disc have been reported from LMXBs containing a NS (e.g. Bhattacharyya & Strohmayer 2007; Iaria et al. 2009; D'Aì et al. 2009). All the *XMM-Newton* observations where a broad skewed Fe line has been reported were included in our sample (see Sect. 4). However, in contrast to previous analyses, we *do not* need to invoke relativistic effects to explain its width, which could be due to mechanisms such as Compton broadening. The lines are *equally well* fitted with the relativistic `laor` component or with a simpler Gaussian component. Furthermore, the profiles shown in Fig. 3 do not show any asymmetric shape, as expected if the lines are emitted close to the NS and shaped by relativistic effects. The line profile is instead symmetric, similar to the one found in dipping sources (Díaz Trigo et al. 2006). The major difference between the analysis presented in this work and previous works is a careful treatment of pile-up effects, common in the observations of bright LMXBs, and a different modelling of the continuum in some cases, which has a strong effect on the *EW* of the lines.

As shown by Brandt & Matt (1994), in a scenario where the Fe line is generated at the inner disc, we would expect the centroid and the width of the Fe line to decrease as the accretion rate diminishes and the disc recedes. The behaviour of the *EW* is somewhat more complex, because the line's *EW* is expected to first increase with ξ up to a certain value where it starts to decrease (see Fig. 5b from Brandt & Matt 1994). This comes from the emission properties of Fe atoms as a function of the ionisation parameter (Matt et al. 1994). When the most abundant ions are Fe XXIV–Fe XXVI, line emission is more intense than in the neutral case, owing to the greater fluorescent yield and the smaller photoabsorption cross-section at the line

energy. However, if ξ increases further, the ion distribution becomes dominated by fully stripped atoms, and the line emission decreases. In the observations presented in this paper, we do not observe a correlation between the centroid and the width of the Fe line with luminosity, in agreement with a similar systematic analysis based on ASCA observations (Asai et al. 2000). In contrast, the three cases for which a large width and *EW* are measured occur at relatively low luminosities and are actually associated to large errors. This seems to be at odds with the behaviour predicted by Brandt & Matt (1994) for lines generated at the disc and suggests instead that the physical condition of the line-emitting region is rather similar among the LMXBs.

An interpretation of the line in the context of disc emission would imply that the line is produced far from the neutron star to explain its symmetric shape. However, in such a case, it is difficult to justify the variations in the line as the disc inner radius changes.

Alternatively, the origin of the line broadening could be Compton scattering in a corona. Based on a systematic analysis of twenty NS LMXBs with ASCA, Asai et al. (2000) conclude that the Fe lines were likely produced through the radiative recombination of photoionised plasma, and the line width is a result of the combination of line blending, Doppler broadening, and Compton scattering. Combining such effects, Kallman & White (1989) estimated that *EW*s of up to 100 eV were attainable from an ADC using standard parameters. This agrees with the values obtained in this work.

Finally, the line could originate in a partially ionised wind as a result of illumination by the central source continuum photons and broadened by electron downscattering in the wind environment (e.g., Laurent & Titarchuk 2007; Titarchuk et al. 2009). The line profiles obtained via such a mechanism are again asymmetric, similar to the ones produced by relativistic effects. Since the line profiles obtained here are highly symmetric, we do not attribute the line origin to the outflow based on these observations.

5.2. Continuum emission

The X-ray continua for 80% of the observations were well fitted by a model consisting of a blackbody and disc-blackbody components absorbed by neutral material. For 15% of the observations, a model consisting of a blackbody and power law components absorbed by neutral material was preferred to the combination of blackbody and disc-blackbody components. For one observation, a fit with three components, namely,

blackbody, disc-blackbody, and power law, was required to get an acceptable χ^2_ν.

For the fits with blackbody and disc-blackbody components, the temperature of the blackbody component had values between 1.5 and 2.8 keV, except for 4U 1728−34, for which a temperature of $3.8^{+8.4}_{-1.1}$ keV was found. The temperature of the disc blackbody component had lower values between 0.6 and 1.3 keV, except for 4U 1728−34, for which a temperature of 1.9 ± 0.3 keV was found. This is consistent with the interpretation of the blackbody component as the boundary layer between the neutron star and the inner disc, which shows smaller radii and higher temperatures. Based on an ASCA survey, Church & Balucińska-Church (2001) found a broad dependence of the blackbody luminosity on the total luminosity, not previously known for LMXBs in general; but while they found that the blackbody luminosity was falling more rapidly than the total luminosity as the mass accretion rate decreases, we find a very tight correlation where the blackbody luminosity is very near the value of 50% of total luminosity at all luminosities. This may be due to the different continuum model used, blackbody and cutoff power law components (Church & Balucińska-Church 2001) versus blackbody, and disc blackbody components (this work). Similar to Church & Balucińska-Church (2001), we find that the major change in blackbody emission results primarily from changes in the emitting area, not the temperature. The independence of the temperature of this component on the global value of Eddington ratio lends support to the theoretical suggestion that the boundary layer is radiation-pressure-supported (Inogamov & Sunyaev 1999; Revnivtsev & Gilfanov 2006).

For the sources fitted with blackbody and power law components, the temperature of the blackbody component had values between 0.6 and 2.2 keV and the index of the power law was between 1.8 and 2.6.

We detected an excess of emission at ∼1 keV in *all* the observations where we could use the spectrum down to 0.7 keV, except for the two accreting millisecond pulsars XTE J1807−294 and SAX J1808.4−3658. We modelled such emission with a Gaussian component centred between 1.0 and 1.15 keV in 12 observations and as an edge between 0.84 and 0.86 keV in 2 observations. Provided the feature has an astrophysical origin, appearing always at the similar energy points to line emission, since a soft component due to a, say, blackbody emission is expected to change its temperature for different sources. Its energy is consistent with emission from highly ionised Fe, from Fe XX to Fe XXIV, and/or Ne X. We did not find any clear correlation between the width of the line emission at ∼1 keV and the Fe Kα band. However, the fact that the same feature is not observed in simultaneous EPIC and RGS exposures (e.g. Boirin et al. 2005) indicates that the feature is likely blended emission from various ions and additionally broadened by the same mechanism as the Fe Kα line.

In this work, we show that effects of pile-up can significantly affect the width, hence the physical interpretation, of the Fe line in NS X-ray binaries. Furthermore, parallel works on *XMM-Newton* and *Suzaku* observations of the black hole X-ray binary GX 339-4 demonstrate that, taking pile-up effects into account, the breadth of the line is consistent with a truncation of the disc (Done & Díaz Trigo 2010) or with a black hole with moderate spin (Yamada et al. 2009), in contrast to previous claims (e.g. Miller et al. 2006, 2008). Therefore, we urge caution in using piled-up data for detailed spectral analysis.

References

Arnaud, K. A. 1996, in Astronomical Data Analysis Software and Systems V, ASP Conf. Ser., 101, 17
Asai, K., Dotani, T., Nagase, F., & Mitsuda, K. 2000, ApJS, 131, 571
Bhattacharyya, S., & Strohmayer, T. 2007, ApJ, 664, 103
Boirin, L., & Parmar, A. N. 2003, A&A, 407, 1079
Boirin, L., Parmar, A. N., Barret, D., Paltani, S., & Grindlay, J. E. 2004, A&A, 418, 1061
Boirin, L., Méndez, M. Díaz Trigo, M., Parmar, A. N., & Kaastra, J. 2005, A&A, 436, 195
Brandt, W. M., & Matt, G. 1994, MNRAS, 268, 1051
Cackett, E. M., Miller, J. M., Bhattacharyya, S., et al. 2008, ApJ, 674, 415
Cackett, E., Altamirano, D., Patruno, A., et al. 2009, ApJ, 694, L21
Cackett, E. M., Miller, J. M., Ballantyne, D. R., et al. 2010, ApJ, 720, 205
Casares, J., Cornelisse, R., Steeghs, D., et al. 2006, MNRAS, 373, 1235
Church, M. J., & Balucińska-Church, M. 2001, A&A, 369, 915
D'Aì, A., Di Salvo, T., Iaria, R., et al. 2006, A&A, 448, 817
D'Aì, A., Di Salvo, T., Matt, G., & Robba, N. R. 2009, ApJ, 693, L1
D'Aì, A., Di Salvo, T., Ballantyne, D., et al. 2010, A&A, 516, A36
Den Herder, J. W., Brinkman, A. C., Kahn, S. M., et al. 2001, A&A, 365, L7
Di Salvo, T., D'Aì, A., Iaria, R., et al. 2009, MNRAS, 398, 2022
Díaz Trigo, M., Parmar, A. N., Boirin, L., Méndez, M., & Kaastra, J. 2006, A&A, 445, 179
Done, C., & Díaz Trigo, M. 2010, MNRAS, 407, 2287
Done, C., Sobolewska, M. A., Gierliński, M., & Schurch, N. J. 2007, MNRAS, 374, L15
Fabian, A. C., Rees, M. J., Stella, L., & White, N. E. 1989, MNRAS, 238, 729
Fabian, A., & Miniutti, G. 2005, in The Kerr Spacetime, ed. D. L. Wiltshire, M. Visser, & S. M. Scott
Galloway, D. K., Muno, M. P., Hartman, J. M., Psaltis, D., & Chakrabarty, D. 2008, ApJS, 179, 360
Grimm, H. J., Gilfanov, M., & Sunyaev, R. 2002, A&A, 391, 923
Guainazzi, M., Bianchi, S., & Dovciak, M. 2006, Astron. Nachr., 327, 1032
Hasinger, G., van der Klis, M., Ebisawa, K., Dotani, T., & Mitsuda, K. 1990, A&A, 235, 131
Hiemstra, B., Soleri, P., Méndez, M., et al. 2009, MNRAS, 394, 2080
Hirano, T., Hayakawa, S., Nagase, F., Masai, K., & Mitsuda, K. 1987, PASJ, 39, 619
Iaria, R., Di Salvo, T., Robba, N. R., et al. 2004, ApJ, 600, 358
Iaria, R., D'Aì, A., Di Salvo, T., et al. 2009, A&A, 505, 1143
Inogamov, N. A., & Sunyaev, R. A. 1999, Astron. Lett., 25, 269
Jansen, F., Lumb, D., Altieri, B., et al. 2001, A&A, 365, L1
Kallman, T., & White, N. E. 1989, ApJ, 341, 955
Kuulkers, E., in 't Zand, J. J. M., Atteia, J. L., et al. 2009, A&A, 514, A65
Laming, J. M., & Titarchuk, L. 2004, ApJ, 615, L121
Laurent, P., & Titarchuk, L. 2007, ApJ, 656, 1056
Mason, K. O., Breeveld, A., Much, R., et al. 2001, A&A, 365, L36
Matt, G. 2006, Astron. Nachr., 327, 949
Méndez, M., Cottam, J., & Paerels, F. 2002, in New Visions of the X-ray Universe in the *XMM-Newton* and Chandra Era, ESA SP–488
Miller, J. M., Homan, J., Steeghs, D., et al. 2006, ApJ, 653, 525
Miller, J. M., Reynolds, C. S., Fabian, A. C., et al. 2008, ApJ, 679, L113
Miller, J. M., Reynolds, C. S., Fabian, A. C., Miniutti, G., & Gallo, L. C. 2009, ApJ, 697, 900
Nandra, K., George, I. M., Mushotzky, R. F., Turner, T. J., & Yaqoob, T. 1997, ApJ, 477, 602
Nandra, K., O'Neill, P. M., George, I. M., & Reeves, J. N. 2007, MNRAS, 382, 194
Pandel, D., Kaaret, P., & Corbel, S. 2008, ApJ, 688, 1288

Papitto, A., Di Salvo, T., D'Aì, A., et al. 2009, A&A, 493, L39
Patruno, A., Rea, N., Altamirano, D., et al. 2009, MNRAS, 396, L51
Pozdnyakov, L. A., Sobol, I. M., & Sunyaev, R. A. 1979, A&A, 75, 214
Reis, R. C., Fabian, A. C., Ross, R. R., & Miller, J. M. 2009, MNRAS, 395, 1257
Revnivtsev, M. G., & Gilfanov, M. R. 2006, A&A, 453, 253
Reynolds, C. S., & Nowak, M. A. 2003, Phys. Rep., 377, 389
Ross, R. R., & Fabian, A. C. 2007, MNRAS, 381, 1697
Sidoli, L., Oosterbroek, T., Parmar, A. N., Lumb, D., & Erd, C. 2001, A&A, 379, 540
Strüder, L., Briel, U., Dennerl, K., et al. 2001, A&A, 365, L18
Sunyaev, R. A., & Titarchuk, L. G. 1980, A&A, 86, 121

Tanaka, Y., Nandra, K., Fabian, A. C., et al. 1995, Nature, 375, 659
Titarchuk, L., Kazanas, D., & Becker, P. A. 2003, ApJ, 598, 411
Titarchuk, L., Laurent, P., & Shaposhnikov, N. 2009, ApJ, 700, 1831
Turner, M. J. L., Abbey, A., Arnaud, M., et al. 2001, A&A, 365, L27
Vaughan, S., & Uttley, P. 2008, MNRAS, 390, 421
Vrtilek, S. D., Soker, N., & Raymond, J. C. 1993, ApJ, 404, 696
Wang, Z., & Chakrabarty, D. 2004, ApJ, 616, L139
White, N. E., & Holt, S. S. 1982, ApJ, 257, 318
White, N. E., Peacock, A., Hasinger, G., et al. 1986, MNRAS, 218, 129
Wilms, J., Allen, A., & McCray, R. 2000, ApJ, 542, 914
Yamada, S., Makishima, K., Uehara, Y., et al. 2009, ApJ, 707, L109

Appendix A: Examples of pile-up removal

Figures A.1 and A.2 show the effects of pile-up in the `epatplot` in the bright source GX 349+2 and the dim source 4U 1728−34, respectively. For GX 349+2 we observe a significant energy-dependent deviation between the data and the model ≳4 keV when the full PSF region is used (Fig. A.1, upper left). As we remove the inner columns from the PSF the effects of pile-up are mitigated. After removal of 6 columns, there is still a small deviation above 9 keV. After removal of 8 columns, there is not an energy-dependent deviation anymore (Fig. A.1, right panel). For 4U 1728−34 we do not observe any energy-dependent deviation between the data and the model when the full PSF region is used (Fig. A.2, left panel). Similarly, when we excise the core of the PSF, the pattern ratios do not change with respect to the case where the core of the PSF is included. This indicates that pile-up is not present in this source.

Appendix B: Comparison with previous results

Several sources analysed in this paper have been previously published by other authors (e.g. Bhattacharyya & Strohmayer 2007; Iaria et al. 2009; D'Aì et al. 2009). In what follows, we compare the properties of the Fe Kα line found in previous analyses with the ones inferred in this paper. For most of the sources we obtained significantly different parameters for the Fe line when fitted with a `laor` component, compared to previous analyses (we discuss the discrepancies in detail below).

Therefore, to obtain a quantitative measurement of the difference between the Fe line obtained by other authors and in this work we performed fits to the spectra with the best-fit model shown in Sect. 3.2 but fixing all the parameters of the `laor` component to the values obtained in previous analyses except the normalisation, which was left free. The χ^2_ν of these fits is shown in Table B.1. For comparison, we show in the same table the χ^2_ν obtained when the line is fitted both with a Gaussian and a `laor` component and leaving all the parameters free, as in Tables 3–5. We compared the results in this work with the results obtained by Cackett et al. (2010) only in Table B.1 and not in the sections that follow, since their work is being refereed at the moment of acceptance of this paper, and the parameters may still change in their final version.

We found that the χ^2_ν of the fits to the lines with the parameters of the literature yielded higher values of χ^2_ν for eight of the observations analysed in this work (see Table B.1). For the three observations of 4U 1636−536, the difference in χ^2_ν is not statistically significant. Indeed the lines fitted in this work have a width σ near 1 keV, similar to previous analyses. However, two of the three lines are below the level of 3σ detectability significance in this work, and the third one is only slightly above such limit (see Sect. 4). Also in the case of 4U 1636−536 Obs 0500350401, we obtained a lower, though not significant, χ^2_ν when using the parameters of the line from previous analyses. This is because we did not allow any inclination higher than 70° in our analysis, since the source shows neither dips nor eclipses. In contrast, the value of the inclination in the `laor` component in previous analyses had a higher value of >81° (e.g., Pandel et al. 2008; Cackett et al. 2010). For the observations of Ser X−1, SAX J1808.4−3658, and GX 340+0, the increase in the χ^2_ν when we use the parameters of the lines in the literature is not statistically significant, since the χ^2_ν is already well below 1 in the fits in this work. However, since the χ^2_ν is already below 1 for fits with the simple Gaussian model, there is no reason to consider a `laor` component for these fits.

B.1. Ser X−1

Bhattacharyya & Strohmayer (2007) first report a skewed Fe Kα line with a moderately extended red wing in an NS LMXB based on the three *XMM-Newton* observations of Ser X−1 that we re-analysed in this paper. They fitted the line with a `laor` component and find *EW*s for the lines between 86^{+9}_{-11} and 105^{+7}_{-8} eV, inner radii between $4.04^{+2.14}_{-0.68}$ and $16.19^{+8.77}_{-3.19}$ r_g, and an energy centroid of $6.4^{+0.08}_{-0.0*}$ keV. On average we found smaller *EW*s, between 57 ± 18 and 63 ± 12 eV, and larger energy centroids, between 6.60 ± 0.1 and $6.79^{+0.1}_{-0.2}$ keV, when fitting the line with the same component and *EW*s between 50^{+14}_{-12} and 52^{+14}_{-11} and an average energy centroid of 6.60 ± 0.04 keV when fitting the line with a Gaussian component. We also inferred a smaller average inclination for the source from the `laor` fit: between <25 and $28 \pm 9°$, compared to between $39.7^{+1.4}_{-1.5}$ and $50.2^{+8.8}_{-5.4}°$ found by Bhattacharyya & Strohmayer (2007). The inner radius was not well constrained when fitting the line with a `laor` component, with a value of $13.3^{+19.3}_{-6.9}$ r_g for the best-constrained observation (Obs 0084020401). In our analysis the fit with the `laor` component was not statistically preferred to the one with the Gaussian component.

We explain the discrepancies in the results as mainly due to two differences in the analysis. First, while Bhattacharyya & Strohmayer (2007) consider pile-up to be insignificant for these observations, we found that the `epatplot` shows a significant degree of pile-up before we remove the central 4 columns of the PSF. Figure B.1 shows the difference in the spectra extracted when including the core of the PSF, as done by Bhattacharyya & Strohmayer (2007), and excluding the 4 central columns to remove pile-up effects, as in this paper. The pile-up effects show up as an excess of photons from as low as 3 keV and becomes especially prominent above 5 keV in the red spectrum. This, combined with a improper continuum modelling (see below), may create an excess of photons below 6 keV, which could be misinterpreted as a red wing of the Fe line.

The second difference in the analysis is precisely that we used a different continuum model to fit the spectrum. As shown in Table 6 we got a significantly worse χ^2_ν using a combination of `diskbb` and `comptt` components to fit the continuum, as done by Bhattacharyya & Strohmayer (2007), when compared to `diskbb` and `bbody` components used in this paper.

Therefore, for this particular source, the main contribution to the broad Fe line detected in the first analysis by Bhattacharyya & Strohmayer (2007) is likely related to residuals from the fit to the continuum, showing that modelling the spectra with different continua may significantly modify the parameters of the Fe line.

B.2. GX 340+0

D'Aì et al. (2009) report a broad asymmetric emission line in the *XMM-Newton* spectrum of GX 340+0. Owing to the variability of the source as revealed by the light curve (see Fig. 2), they divided the observation into five segments and analysed each segment separately. They modelled the spectral continuum with `diskbb` and `bbody` components and find a significant improvement in the fit when using the `diskline` component to model the Fe Kα emission compared to a Gaussian component. The line had an average energy of 6.69 ± 0.02 keV, inner radius of 13 ± 3 r_g, and *EW* of 41 ± 3 eV. In spite of using the same continuum to model the spectrum, we obtained equally good fits when modelling the Fe line with a Gaussian or with a `laor` component. The line had an average energy of $6.82^{+0.07}_{-0.13}$ keV,
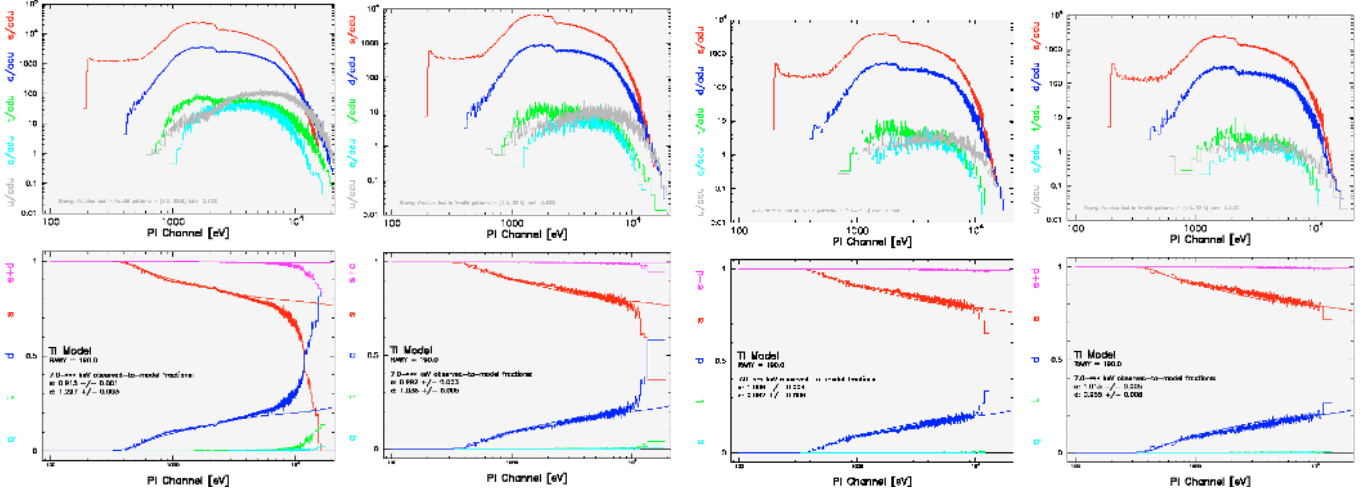
Fig. A.1. Measure of pile-up in the EPIC pn timing mode using the SAS task `epatplot` for the bright source GX 349+2. Source events were extracted from a 64″ (16 columns) wide box centred on the source position (left panel). Middle-left, middle-right, and right panels show the same region as in the left panel but after exclusion of the neighbouring 4, 6, and 8 columns from the centre of the box.
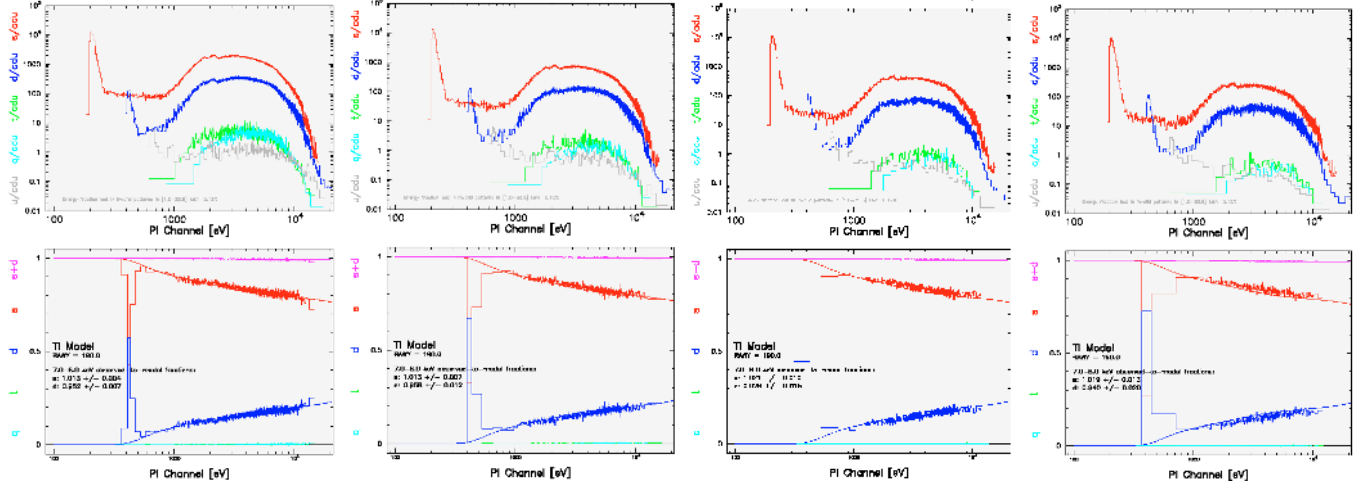

Fig. A.2. Same as Fig. A.1 but for the dim source 4U 1728−34.

an inner radius >16 r_g, and a smaller *EW* of 15 ± 5 eV. We inferred an average inclination for the source of <34°, compared to 35 ± 1° found by D'Aì et al. (2009). When fitted with a Gaussian profile, the line had an energy of 6.76 ± 0.02 keV and width of 0.24 ± 0.02 keV (D'Aì et al. 2009), consistent with our values of 6.72 ± 0.06 keV and width of $0.17^{+0.14}_{-0.08}$ keV.

The main difference bewteen our analysis and theirs is again the treatment of pile-up. While they only considered the initial ~7 ks of the observation (interval 5) to be affected by pile-up and excised the 2 central columns to remove its effects, we found that the full observation was strongly affected by pile-up so removed the central 8 columns. This is consistent with the high count rate of the source, with peaks up to ≳1100 counts s^{-1} and a minimum of 650 counts s^{-1} along the observation, as well as the hardness of the spectrum (see Sect. 2.1). The light curve in this paper (see Fig. 2) shows a count rate twice as high as the one shown in Fig. 1 from D'Aì et al. (2009). A potential explanation of this difference in the light curves could be that D'Aì et al. (2009) averaged intervals of real data with those for which no data were recorded, because of telemetry saturation.

B.3. GX 349+2

Iaria et al. (2009) report several emission features, consistent with the transitions of L-shell Fe XXII-Fe XXIII, S XVI, Ar XVIII, Ca XIX, and highly ionised Fe in the *XMM-Newton* spectrum of GX 349+2. While the first four features can be fitted equally well with Gaussian features or the relativistic `diskline` component, they find that the Fe Kα feature is better fitted using the `diskline` component at 6.76 keV or two `diskline` components at 6.7 and 6.97 keV. The line had an energy of 6.80 ± 0.02 keV, width (σ) of $0.28^{+0.03}_{-0.04}$ keV, and *EW* of 49^{+6}_{-7} eV when modelled with a Gaussian component. The same line had an energy of 6.76 ± 0.02 keV, inner radius $6.2^{+19.1}_{-0.2}$ r_g, and *EW* of 61 ± 9 eV when modelled with a `diskline` component.

In spite of using the same continuum to model the spectrum, we obtained equally good fits when modelling the Fe line with a Gaussian or with a `laor` component and a significantly larger *EW* in any of the fits, compared to Iaria et al. (2009). In this paper, the line has an energy of 6.72 ± 0.06 keV, width (σ) of $0.32^{+0.11}_{-0.07}$ keV and *EW* of 82^{+22}_{-15} eV when modelled with a Gaussian component and energy of $6.94^{+0.03}_{-0.22}$ keV, inner radius

Table B.1. χ^2_ν of spectral fits for sources for which asymmetric Fe lines showing relativistic effects reported in the literature.

Source	Observation ID	a	b	c
4U 1636−536	0303250201	0.76 (216)	0.78 (214)	0.85 (218)[1]; 0.84 (218)[2]
	0500350301	0.71 (217)	0.70 (215)	0.71 (219)[1]; 0.70 (219)[2]
	0500350401	0.72 (217)	0.80 (215)	0.69 (219)[1]; 0.69 (219)[2]
GX 340+0	0505950101	0.86 (163)	0.88 (161)	0.98 (165)[3]
GX 349+2	0506110101	1.15 (216)	1.14 (214)	1.37 (218)[1]; 1.30 (218)[4]
4U 1705−44	0402300201	1.01 (186)	1.03 (184)	1.10 (188)[1]
	0551270201	1.07 (187)	1.03 (185)	1.37 (188)[5]
Ser X−1	0084020401	0.98 (216)	0.97 (214)	1.00 (218)[1]; 1.04 (218)[6]
	0084020501	0.93 (216)	0.92 (214)	0.95 (218)[1]; 0.97 (218)[6]
	0084020601	1.04 (216)	1.04 (214)	1.04 (218)[1]; 1.05 (218)[6]
SAX J1808.4−3658	0560180601	0.86 (220)	0.84 (218)	0.88 (222)[7]; 0.92 (222)[8]; 0.90 (222)[9]

Notes. Columns (a) and (b) show the χ^2_ν of the fit after including a Gaussian and a `laor` component, respectively, to the best-fit model. Column (c) shows the χ^2_ν of the fit after including a `laor` component with all the parameters fixed to the values obtained by previous authors, except the normalisation, to the best-fit model.
References. [1] Cackett et al. (2010); [2] Pandel et al. (2008); [3] D'Aì et al. (2009); [4] Iaria et al. (2009); [5] Di Salvo et al. (2009); [6] Bhattacharyya & Strohmayer (2007); [7] Cackett et al. (2009); [8] Patruno et al. (2009); [9] Papitto et al. (2009).
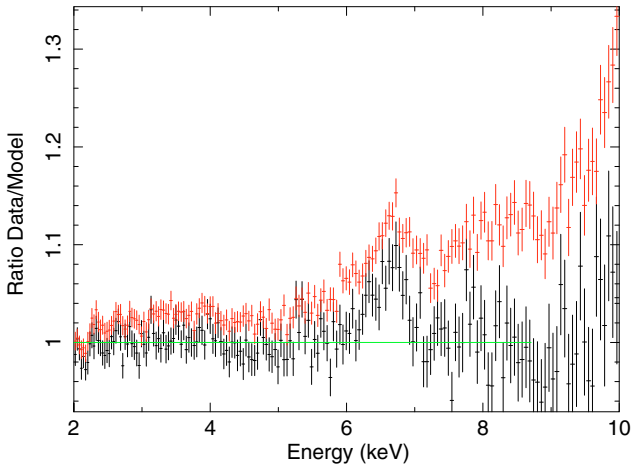

Fig. B.1. Ratio of the EPIC pn spectrum of Ser X−1 (Obs 0084020501) to its best-fit continuum model for the spectrum free of pile-up used in this paper (black). The red points show the ratio of the piled-up spectrum of the same observation, obtained when the full PSF is used, to the best-fit continuum model of the spectrum free of pile-up. The pile-up shows up mainly as a significant hardening of the spectrum at energies $\gtrsim 5$ keV. This adds an "artificial" red-wing to the Fe line because of the different curvature of the spectrum.

of 11^{+7}_{-5} r_g, and *EW* of 96^{+20}_{-14} eV when modelled with a `laor` component. We obtained a significantly different inclination for the source, $17 \pm 9°$, compared to $41.4^{+1}_{-2.1}°$ (Iaria et al. 2009). Apart from the inclination and the *EW*, the line parameters were not significantly different within the errors. We attribute the differences in some properties of the line to the PSF extraction regions used. While Iaria et al. (2009) exclude only the 2 central pixels of the PSF before spectral extraction, their Fig. 4 shows an excess of double events and a deficit of single events above ~7.5 keV compared to the predicted model. This is a clear indication of residual pile-up in their spectra (see *XMM-Newton Users Handbook*). In contrast, we found that rejection of the inner 8 columns of the PSF was necessary in order to completely remove the pile-up effects.

We found a lower temperature for the `diskbb` and `bbody` components, 0.92 ± 0.03 and 1.57 ± 0.02 keV, compared to $1.05^{+0.02}_{-0.03}$ and $1.792^{+0.006}_{-0.019}$ keV (Iaria et al. 2009). Thus the spectrum extracted in this paper is significantly softer compared to the analysis by Iaria et al. (2009). Again, this is expected if pileup effects have not been completely removed from the spectra in their analysis.

B.4. 4U 1705−44

4U 1705−44 was observed twice by *XMM-Newton* with the EPIC pn camera in timing mode. The first observation had a relatively low flux, 2.5×10^{-10} erg cm^{-2} s^{-1}, and was at least one order of magnitude below the typical count rate where pileup effects become important. In 2008 *XMM-Newton* observed 4U 1705−44 at a significantly higher flux, 642 counts s^{-1} compared to 28 counts s^{-1} in 2006 (see Table 1). Di Salvo et al. (2009) report four emission features and one absorption edge in the spectral residuals after modelling the continuum with a `bbody` and a `comptt` components, which were identified with emission of S XVI, Ar XVIII, Ca XIX, and Fe XXV, and (redshifted) absorption from Fe XXV. The lines were broad with σ between 120 and 260 eV. They find a significant improvement in the fit when the Fe XXV feature is modelled with a `diskline` component compared to a Gaussian component and reported values of 6.66 ± 0.01 keV, 14 ± 2 r_g, 39 ± 1 and 56 ± 2 eV for the energy, inner radius, inclination, and *EW* for the fit with a `diskline` component. The absorption edge appeared to be smeared (width of 0.7 keV) and redshifted with an energy of 8.3 ± 0.1 keV with respect to the rest frame energy of 8.83 keV. We found values of 6.45 ± 0.05 keV, <9 r_g, $<34°$, and 135^{+10}_{-21} eV for the energy, inner radius, inclination and *EW* for the fit with a `laor` component, i.e. significantly different to those reported by Di Salvo et al. (2009). When fitted with a Gaussian component, the centroid was 6.56 ± 0.05 keV and the *EW* 92^{+23}_{-8} eV.

The difference between both analyses is again related to both the pile-up treatment and the modelling of the continuum. We found that it was necessary to excise the 7 central columns of the PSF to completely remove pile-up effects, while Di Salvo et al. (2009) did not remove any column. In addition,

Di Salvo et al. (2009) used a continuum of `bbody` and `comptt` to fit the spectrum, while we used `bbody` and `diskbb`.

B.5. SAX J1808.4−3658

SAX J1808.4−3658 was observed by *XMM-Newton* in 2008 and its spectrum modelled with a combination of `diskbb`, `blackbody`, and `power law` components (Papitto et al. 2009; Patruno et al. 2009; Cackett et al. 2009). The residual emission at the Fe Kα band is modelled with a `diskline` profile in all the analyses, although Papitto et al. (2009) obtained only a slight improvement in the fit when using a `diskline` profile compared to a Gaussian profile. The parameters of the `diskline` component were in general consistent in the three analyses, with some exceptions such as the inclination derived for the source, probably because of small differences in the analyses such as including the RGS in the simultaneous fit or not or considering slightly different energy bands. For example, Papitto et al. (2009) (Cackett et al. 2009) used the 1.4−11 keV (1.2−11 keV) band for spectral fitting, since they found large residuals below 1.4 (1.2) keV, respectively.

As explained in Sect. 3.2 we extracted two different spectra for this observation. Spectrum 1 was extracted including the core of the PSF, as done by the authors above. Despite using the same extraction region, we found a significantly smaller line, with an *EW* of 51^{+20}_{-16} eV when fitting the line with a `laor` component and 23^{+9}_{-7} eV in the fits with a Gaussian component. In contrast, in the previous analyses with a `laor` component, the *EW* was found to be as large as 121^{+20}_{-16} eV (Papitto et al. 2009), 118 ± 10 (Cackett et al. 2009), and 97.7 ± 31.4 eV (Patruno et al. 2009).

This may be related to the different continuum used to fit the spectrum. While all the previous analyses of the *XMM-Newton* observation of SAX J1808.4−3658 required 3 continuum components to achieve an acceptable fit, we already obtain a χ^2_ν of 0.98 (223) with a continuum consisting of just blackbody and power-law components.

B.6. 4U 1636−536

Pandel et al. (2008) find evidence for relativistic lines from Fe in different ionisation states in the three *XMM-Newton* observations of 4U 1636−536 presented here. They report *EW*s of 215, 98, and 140 eV for the Fe Kα line present in Obs 0303250201, 0500350301, and 0500350401, respectively, which they modelled with a `diskline` component. In contrast, we found smaller *EW*s of 130 ± 14, 36^{+34}_{-16}, and 6 ± 3 eV when fitting the line with a `laor` component and of 210 ± 129, 28 ± 19, and 59^{+15}_{-17} eV when using a Gaussian component instead. When fitting the line with a Gaussian component, the lines from Obs 0303250201 and 0500350301 are below the 3σ significance level so should not be considered as detections. Pandel et al. (2008) regard the high inclination, >81°, obtained for Obs 0303250201 and 0500350401 as unrealistic (given the values of the inclination of 36−74° determined for this source Casares et al. (2006)) and interpreted it as an indication that the excess at the Fe Kα band was a blend of at least two lines. In contrast, we found only a high inclination for Obs 0303250201 and an upper value of 70° (as used for all the fits in this sample) already gave an acceptable fit with a χ^2_ν of 0.76 (216) for this observation. We obtained equally good fits when modelling the Fe line with a Gaussian or with a `laor` component.

We attribute the differences in some properties of the line to the PSF extraction regions used. Pandel et al. (2008) consider that none of the three *XMM-Newton* observations suffer from pile-up effects based on the count rate limit for the pn timing mode. In contrast we found that rejection of the inner 1(3) columns of the PSF was necessary in order to remove the pile-up effects completely for Obs 0500350301 (0500350401). The residual pile-up effects in their spectra are most likely responsible for the harder spectrum. They report a difference of their spectra with respect to the simultaneous RXTE PCA spectra both of flux and slope. The PCA spectra show a flux excess of ∼30% at 3 keV and ∼10−15% at 10 keV with respect to their EPIC pn spectra. Qualitatively, this is what we expect if the *XMM-Newton* spectra are affected by pile-up: photons will be lost so that in average the flux is lower and in addition soft photons will be counted as hard photons, so that in average the PCA will show a softer spectrum.

Appendix C: Spectra

The best fits of each individual spectrum, together with the residuals of the fits, are shown in Fig. C.1. Figure C.2 shows the unfolded spectra for each observation.
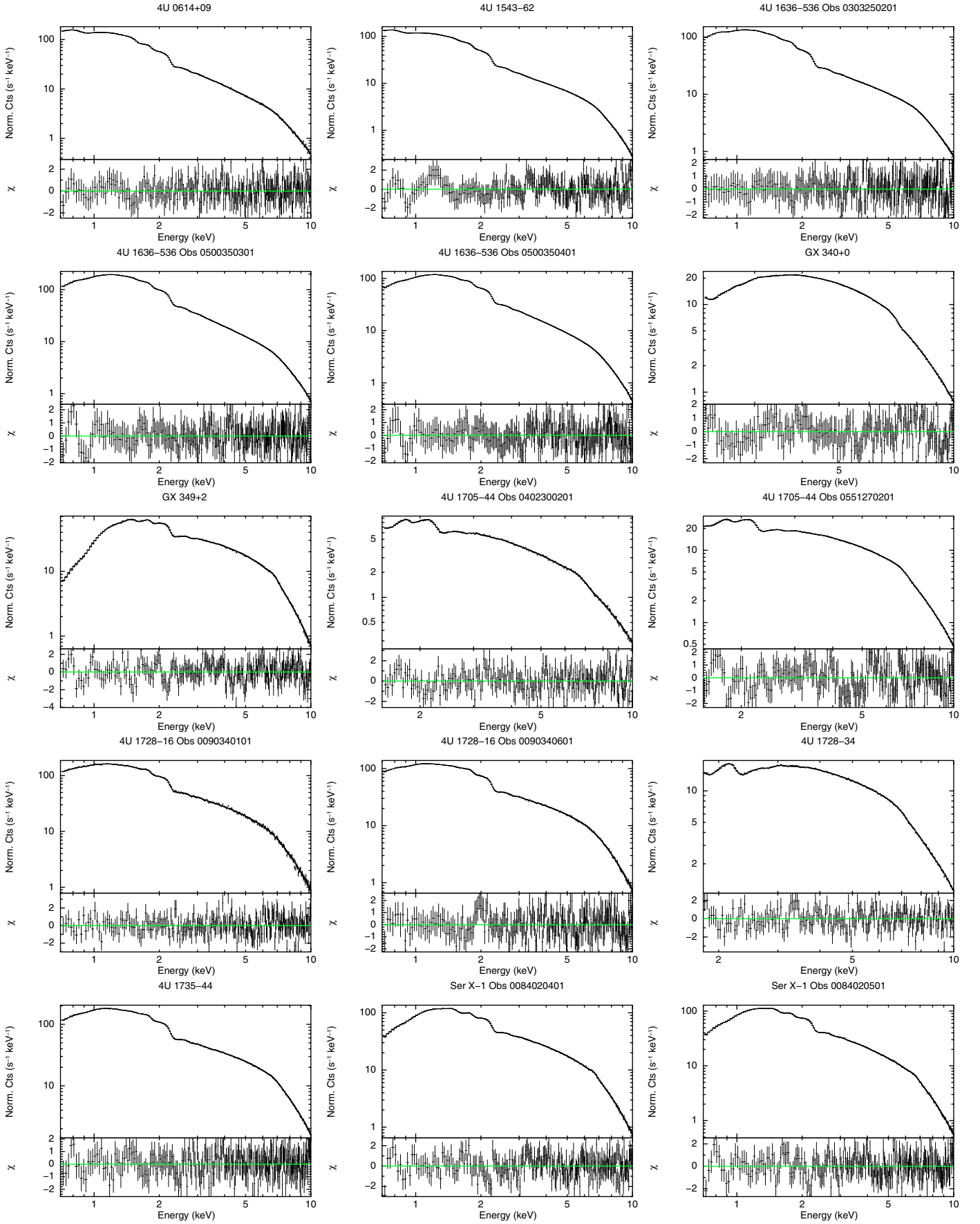
Fig. C.1. *Upper panels*: 0.7−10 keV EPIC pn (black) spectra fit with Models 1a–1d. For each source the best fit is shown (see Tables 3−4 and text). *Lower panels*: residuals in units of standard deviation from the corresponding model.
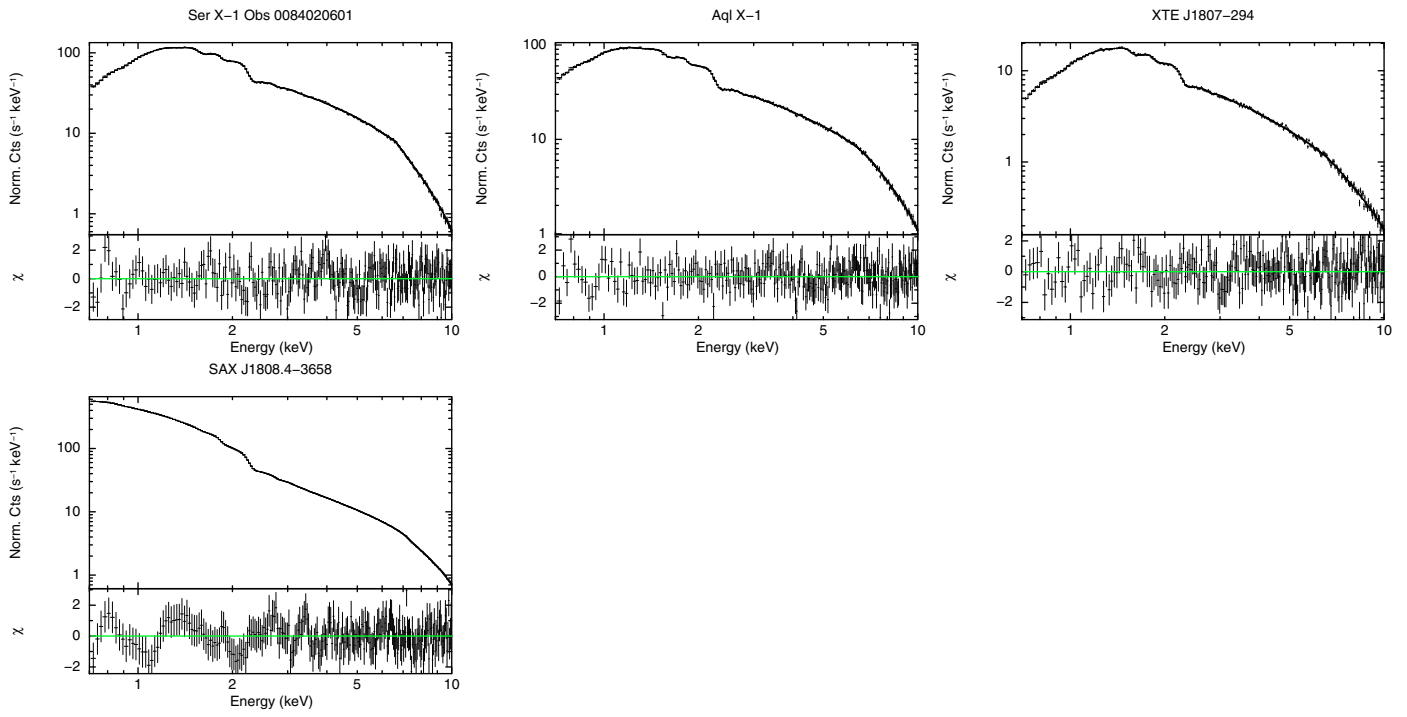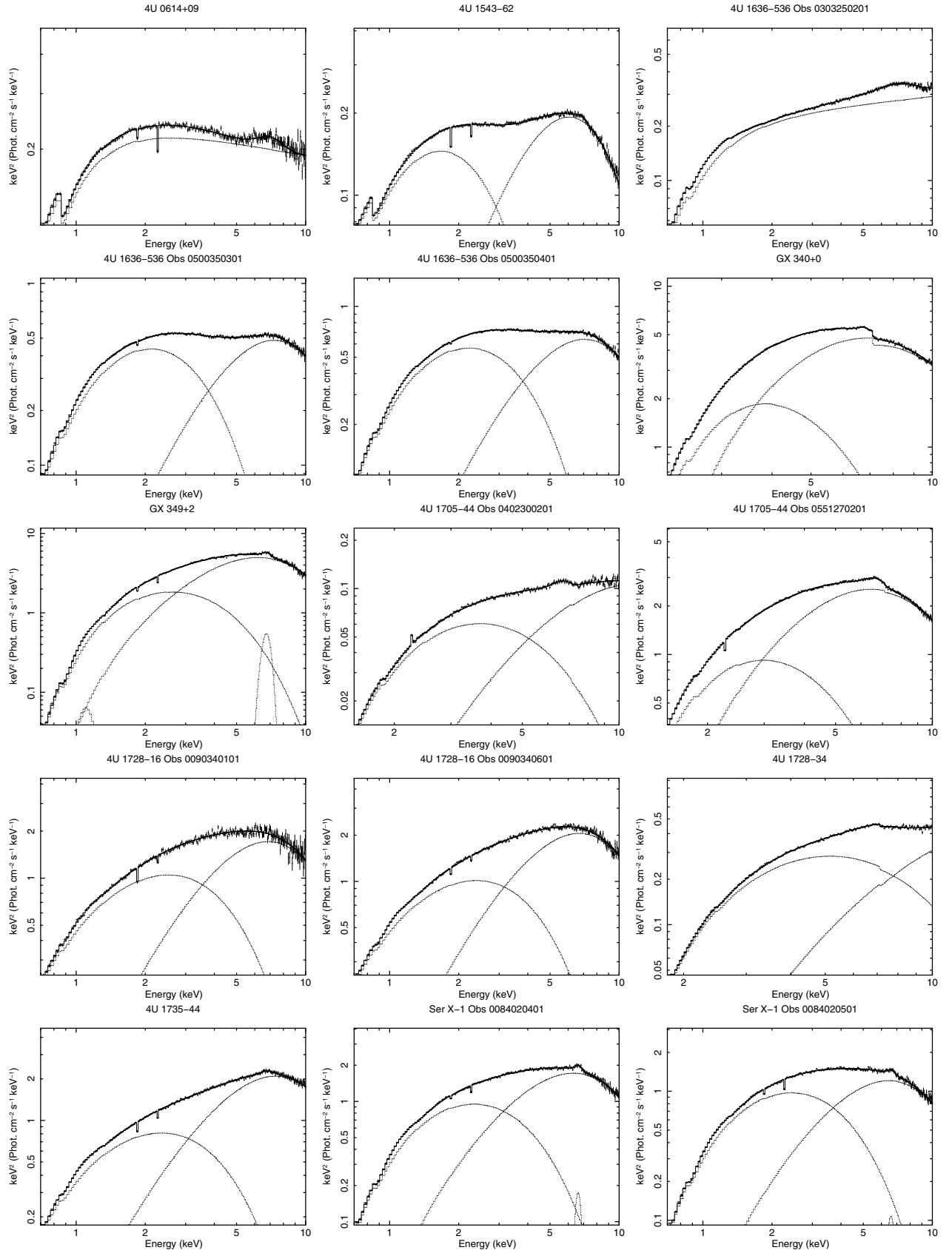
Fig. C.1. continued.

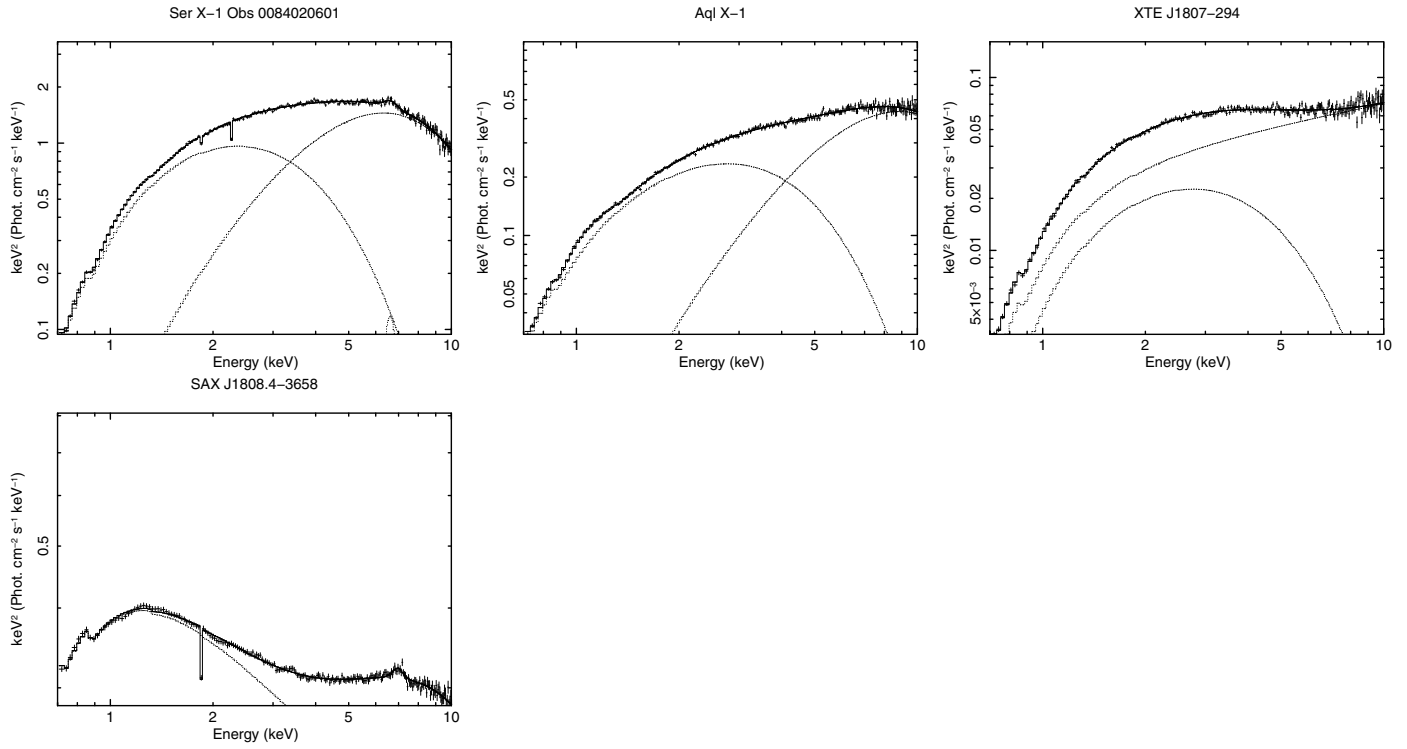**Fig. C.2.** 0.7–10 keV EPIC pn (black) spectra fit with their best-fit model (see Tables 3, 4) shown in flux units.

Fig. C.2. continued.